

The role of lithospheric thickness in the formation of ocean islands and seamounts: contrasts between the Louisville and Emperor-Hawaiian hotspot trails

J. Godfrey Fitton¹, Rebecca Williams², Tiffany L. Barry³ and Andrew D. Saunders³

1. School of GeoSciences, University of Edinburgh, Grant Institute, West Mains Road, Edinburgh EH9 3JW, UK (corresponding author; 0131 650 8529; godfrey.fitton@ed.ac.uk)
2. Department of Geography, Geology and Environment, University of Hull, Cottingham Road, Hull HU6 7RX, UK
3. School of Geography, Geology and the Environment, University of Leicester, University Road, Leicester LE1 7RH, UK

Running title: Magmatism in the Louisville and Emperor seamounts

ABSTRACT

The Hawaii-Emperor and Louisville seamounts form the two most prominent time-progressive hotspot trails on Earth. Both formed over a similar time interval on lithosphere with a similar range of ages and thickness. The Hawaii-Emperor seamounts are large and magma productivity appears to be increasing at present. The Louisville seamounts, by contrast, are smaller and the trail appears to be waning. We present new major- and trace element data from five of the older (74-50 Ma) Louisville seamounts drilled during International Ocean Drilling Program (IODP) Expedition 330 and compare these to published data from the Emperor seamounts of the same age. Despite drilling deep into the shield-forming volcanic rocks at three of the Louisville seamounts, our data confirm the results of earlier studies based on dredge samples that the Louisville seamounts are composed of remarkably uniform alkali basalt. The basalt composition can be modelled by $\sim 1.5\text{--}3\%$ partial melting of a dominantly garnet lherzolite mantle with a composition similar to that of the Ontong Java Plateau mantle source. Rock samples recovered by dredging and drilling on the Emperor Seamounts range in composition from tholeiitic to alkali basalt and require larger degrees of melting (2–10%) and spinel- to garnet lherzolite mantle sources. We use a simple decompression melting model to show that melting of mantle with a potential temperature of 1500°C under lithosphere of varying thickness can account for the composition of the shield-forming tholeiitic basalts from the Emperor seamounts, while post-shield alkali basalt requires a lower temperature ($1300\text{--}1400^\circ\text{C}$). This is consistent with the derivation of Hawaii-Emperor shield-forming magmas from the hotter axis of a mantle plume and the post-shield magmas from the cooler plume sheath as the seamount drifts away from the plume axis. The composition of basalt from the Louisville seamounts shows no significant variation with lithosphere thickness at the time of seamount formation, contrary to the predictions of our decompression melting model. This lack of influence of lithospheric thickness is

characteristic of basalt from most ocean islands. The problem can be resolved if the Louisville seamounts were formed by dehydration melting of mantle containing a small amount of water in a cooler plume. Hydrous melting in a relatively cool mantle plume ($T_p=1350\text{--}1400^\circ\text{C}$) could produce a small amount of melt and then be inhibited by increasing viscosity from reaching the dry mantle solidus and melting further. The failure of the plume to reach the dry mantle solidus or the base of the lithosphere means that the resulting magmas would have the same composition irrespective of lithosphere thickness. A hotter mantle plume ($T_p\approx 1500^\circ\text{C}$) beneath the Emperor seamounts and the Hawaiian Islands would have lower viscosity before the onset of melting, melt to a larger extent, and decompress to the base of the lithosphere. Thus our decompression melting model could potentially explain the composition of both the Emperor and Louisville seamounts. The absence of a significant lithospheric control on the composition of basalt from nearly all ocean islands suggests that dehydration melting is the rule and the Hawaiian islands the exception. Alternatively, many ocean islands may not be the product of mantle plumes but instead be formed by decompression melting of heterogeneous mantle sources composed of peridotite containing discrete bodies of carbonated and silica-oversaturated eclogite within the general upper mantle convective flow.

Keywords: basalt; decompression melting; mantle plumes; Pacific Ocean; seamounts.

INTRODUCTION

The idea that intraplate hotspots are caused by convective plumes originating in the deep mantle was proposed by Morgan (1971) to explain long, time-progressive chains of ocean islands and seamounts such as the Hawaii-Emperor seamount trail (HEST, Fig. 1). The Louisville seamount trail (LST, Fig. 1) in the southwest Pacific Ocean is another example and was the subject of Integrated Ocean Drilling Program (IODP) Expedition 330. It has been

suggested (e.g. Mahoney and Spencer, 1991) that the LST and the 122 Ma Ontong Java Plateau (OJP) represent, respectively, the tail and head of the same mantle plume.

The primary objective of IODP Expedition 330 was to determine whether the Louisville mantle plume had remained fixed with respect to the Earth's spin axis or whether it had drifted like the Hawaiian plume. Palaeomagnetic studies on drill core recovered from the Emperor seamounts during Ocean Drilling Program (ODP) Leg 197 showed a $\sim 15^\circ$ southwards movement of the Hawaiian hotspot between 81 and 47 Ma (Tarduno et al., 2003). Five of the Louisville seamounts with similar ages were drilled during IODP Expedition 330 (Fig. 2a), and palaeomagnetic data show that there has been little or no motion relative to the Earth's spin axis for the Louisville hotspot during this time (Koppers *et al.*, 2012a).

We present major- and trace-element data on samples recovered from the LST during IODP Expedition 330 and compare them with published data from the HEST (Regelous et al., 2003; Huang et al., 2005). The two suites of samples are of comparable age (74–50 Ma for LST; 85–47 Ma for HEST) and were erupted onto lithosphere with apparently similar age ranges (~ 13 –76 Ma for LST; ~ 17 –84 Ma for HEST). The ages of the seamounts and their underlying seafloor are shown in Figures 2a and 2b. If the two suites of rocks represent basaltic magma generated by decompression melting in mantle plumes of similar composition, then systematic differences between them should reflect differences in the potential temperature (T_p) of their respective mantle plumes. The objective of the present study is to assess the extent to which decompression melting in plumes with different T_p can account for the difference in composition between the two seamount trails.

THE LOUISVILLE SEAMOUNT TRAIL

The Louisville seamount trail extends 4300 km south-eastwards from the Osborn Seamount (Fig. 2a) and comprises at least 75 individual volcanoes, 50 of them more than 3 km high (Lonsdale, 1988). Their age decreases from ~77 Ma (Koppers *et al.*, 2004) at the northwest end of the chain, where the seamount trail is being subducted beneath the Kermadec trench (Ballance *et al.*, 1989). An extrapolation of the LST suggests that the present position of the hotspot is located near the intersection of the Pacific-Antarctic Ridge and the Eltanin Fracture Zone (Lonsdale, 1988; Watts *et al.*, 1988; Koppers *et al.*, 2012b) although the last magmatism associated with the hotspot is thought to have occurred 1.1 million years ago (Koppers *et al.*, 2004). Forty of the seamounts have flattened tops and form coral-free guyots, but none of the more recent (<12 Ma) seamounts reached sea level. Buchs *et al.* (2018) have shown that the flat tops of the LST guyots formed as shallow-marine shelves comprising lava-fed volcanoclastic deltas, unlike the HEST guyots whose flattened tops formed by erosion and truncation of subaerial volcanic edifices. The difference in mode of formation reflects the smaller size and lower rate of magma eruption in the LST. The LST appears to be in decline (Lonsdale, 1988) unlike the HEST, where magmatic productivity has increased considerably over the past 20 Ma (Wessel, 2016). King and Adam (2014) estimate that the HEST mantle buoyancy flux is nearly an order of magnitude higher than that for the LST. The two seamount trails record similar relative motions between heat source (plume) and the overlying plate during the periods of interest: ~6.5 cm/a from 85–42 Ma for the HEST, and ~7.5 cm/a from 74–50 Ma for the LST.

The LST is divided into two segments by the Wishbone Scarps (Fig. 2a): at ~163°W by the East Wishbone Scarp, which is interpreted to be a remanent transform fault, and at 167°W by the West Wishbone Scarp which may be a former intra-oceanic arc, a fracture zone or a spreading centre (Luyendyk, 1995; Billen and Stock, 2000; Sutherland and Hollis, 2001; Mortimer *et al.*, 2006). To the south-east of the scarps, the seamounts are smaller, more

widely spaced and built on seafloor that was formed at ~50–40 Ma (Lonsdale, 1988; Watts *et al.*, 1988; Lyons *et al.*, 2000). To the north-west of the scarps, crustal ages are less well defined, and the boundaries between crustal areas created by different spreading centres are not well known (Billen and Stock, 2000). At the north-west end of the chain, the Osbourn Trough crosses the LST close to Osbourn Seamount (25.9°S, 175.1° W; Fig. 2a). This trough is thought to be an ancient spreading centre which became extinct at 82–71 Ma (Billen and Stock, 2000), 93–86 Ma (Worthington *et al.*, 2006; Downey *et al.*, 2007), or ~115 Ma (Mortimer *et al.*, 2006). Ferrobasalt recovered approximately 250 km north of the eastern termination of the Osbourn Trough at Deep Sea Drilling Project (DSDP) Sites 595 and 596 (Fig. 2a) yielded a minimum age of 100 Ma (Montgomery and Johnson, 1987), and Sutherland and Hollis (2001) estimated a crustal age at these sites of 132–144 Ma based on the biostratigraphy of the deepest sediments cored. DSDP Site 204 lies less than 50 km north of the western part of the Osbourn Trough (Fig. 2a) but drilling at this site failed to reach basement and the cores yielded no reliable biostratigraphic evidence from which its age can be estimated (Billen and Stock, 2000). The seafloor age contours shown in Figure 2a are based on Müller *et al.* (2008), who assume that spreading on the Osbourn Trough ceased at ~86 Ma.

One of the objectives of Expedition 330 was to recover samples of relatively unaltered basalt for geochemical and isotopic analysis. The LST has been extensively dredged, and work on the dredge samples suggests that the volcanic rocks are predominantly alkaline in composition and remarkably homogeneous through the 80 Myr lifespan of the chain (Cheng *et al.*, 1987; Hawkins *et al.*, 1987; Beier *et al.*, 2011; Vanderkluyzen, 2014). Dredge samples, however, only enable a rather limited assessment of the chemical and isotopic composition of the seamounts for two reasons. Firstly, dredging can only sample the rocks exposed on the surface and these might represent only a late-stage, post-shield phase in the development of

the seamounts. Secondly, dredge samples tend to be altered by long exposure to seawater. Drilling at all of the Expedition 330 sites recovered both fresh and variably altered basalt samples, and three of the sites (U1372, U1374 and U1376) were drilled deep enough to have sampled the shield-forming phase of volcanism, as was similarly achieved at sites along the HEST (Fig. 2b). Thus the chemical composition of samples recovered during Expedition 330 can be compared directly with the data from the HEST reported by Regelous et al. (2003) and Huang et al. (2005).

IODP Expedition 330 drilled five seamounts, spread out along a ~2000 km section of the older part of the LST (Fig. 2a). Only one of these (Burton) had previously been named, and the other four were given informal names by the Expedition 330 shipboard scientists after the four brightest southern hemisphere stars: Canopus, Rigil (from Rigil Kentauri, or Alpha Centauri), Achernar and Hadar. Six sites were drilled on the five seamounts: Canopus (U1372), Rigil (U1373, U1374), Burton (U1376), Achernar (U1375), and Hadar (U1377). In total, 1114 m of sedimentary cover and igneous basement were cored and 806 m were recovered, with drilling reaching, respectively, to depths of 232.9, 65.7, 522.0, 182.8, 11.5, and 53.3 metres below sea floor (mbsf). Retrieved core at each drill site was systematically logged, described and interpreted by shipboard scientists during Expedition 330. Scanned images and descriptions of the core recovered at each site, together with detailed interpretation of the stratigraphic sequences and lithologies, have been published in the Expedition 330 report (Koppers et al., 2012b). A summary of the stratigraphy of each site, based on shipboard studies and subsequent shore-based work and the interpretation of downhole logging, is given in Figure 3. The igneous basement recovered during IODP Expedition 330 is composed mostly of lava flows, monolithic volcanoclastic breccias, hyaloclastite and minor sheet intrusions. Because the flat tops of the guyots formed during the construction of the Louisville seamounts (Buchs et al., 2018) we can be confident that most of

our rock samples represent the shield-forming stage. Only the late-stage tuffs and breccias recovered from Burton, which are separated by a limestone unit from the main volcanic sequence (Fig. 3), could represent a post-shield phase of volcanism. A detailed description of the stratigraphy and an interpretation of the lithofacies at each of the drill sites has been published by Buchs et al. (2018).

PETROGRAPHY AND MINERALOGY

Images and descriptions of samples used for ship-board thin section analysis have been published in the Expedition 330 report (Koppers et al., 2012b). Here, we summarise briefly the petrography based on studies carried out by members of the shipboard party (including JGF and RW) and subsequent work by Dorais (2015) and Dorais and Buchs (2019).

The basalts range from aphyric to highly phyric with phenocryst assemblages commonly of olivine, plagioclase, olivine+clinopyroxene, plagioclase+clinopyroxene and olivine+clinopyroxene+plagioclase. Clinopyroxenes are often zoned, and are largely unaltered. Electron probe analysis shows that most of the pyroxenes are Mg-rich diopside, with some rare wollastonite-rich augite grains (Dorais, 2015). Several clinopyroxene antecrysts were found at Rigil (U1373A-7R1 83-85), the product of incorporation of earlier-formed crystals (e.g. cumulates) into later magmas. Three distinct types of clinopyroxene in post-shield (rejuvenated phase) volcanoclastic rocks on Burton are interpreted as, respectively, phenocrysts and disaggregated crystals from cumulates and mantle xenoliths (Dorais and Buchs, 2019). Olivine is variably altered to iddingsite though unaltered crystals were frequently found (Tejada et al., 2015). Some olivines show strain lamellae, also suggestive of the incorporation of fragments from cumulates (Dorais, 2015). Plagioclase crystals and

volcanic glass in the recovered core varied from fresh (Nichols et al., 2014) to heavily altered to clay. Zeolite- and calcite-filled amygdales are common throughout the core. The only medium-grained rock recovered during the expedition was a holocrystalline, moderately porphyritic dolerite cored in Hole U1375B. Phenocryst phases and their relative proportions in each of the samples used in this study are summarised in Table 1.

ANALYTICAL TECHNIQUES

Ninety-one rock samples were selected from the visibly least altered sections of the drill core. Forty-two of the 91 samples studied are from lava flows, 31 are volcanic breccia, and 12 are from minor intrusions. The rest of the samples (6) are clasts in sedimentary units. One sample of volcanoclastic sediment from Burton (1376-03) consisting of relatively unaltered basaltic clasts cemented by zeolite was included despite having a 22 wt.% loss on ignition (Table 1). Rock types for each of the samples used in this study are given in Table 1. The samples were crushed, hand-picked to remove secondary minerals and altered fragments where possible, and then ground in an agate-lined Tema mill. XRF analyses were carried out on all samples at the University of Edinburgh using techniques similar to those described by Fitton et al. (1998), with modifications noted by Fitton and Godard (2004). Typical values for XRF precision are given by Fitton et al. (1998). Major-element concentrations were determined after fusion with a lithium borate flux containing La_2O_3 as a heavy absorber, by a method similar to that described by Norrish and Hutton (1969). Trace-element concentrations were determined on pressed-powder samples. The fused and pressed samples were analyzed using a PANalytical PW 2404 automatic X-ray fluorescence spectrometer with a Rh-anode X-ray tube. Rare earth and other trace elements were determined on a sub-set of 48 samples using an Agilent 7500s inductively coupled plasma mass spectrometer at the Open University,

with a precision of better than 3%. Samples (including basalt standards BR and W-2 for reference) were prepared by dissolution of 0.1 g of each whole-rock powder with HF and HNO₃, and final dilution to 100 ml with 2% HNO₃, following methods described in detail by Rogers et al. (2006). Drift and background were monitored using acid blanks and international reference standards BR and W-2. Analytical data for the rock samples are given in Table 1 and data for international geochemical standards analysed at the same time are given in Tables 2 and 3.

COMPOSITION OF ROCK SAMPLES FROM THE LOUISVILLE SEAMOUNT TRAIL

A total alkali–silica (TAS) diagram (Fig. 4) is used to compare the Louisville data given here with data from the Emperor Seamounts (Regelous et al., 2003; Huang et al., 2005). Rock samples that are likely to be more altered (LOI>2 wt.%) are excluded from this plot. It is clear from this diagram that most of the LST samples are alkaline whereas more than a third of those from the HEST are tholeiitic. Two samples from Canopus and one from Burton plot clearly in the tholeiitic field, but the rest of the Louisville samples are transitional to alkaline in composition. However, a suite of glass samples covering the same depth range as our samples plot entirely in the alkaline field (Nichols et al., 2014). These data are shown as a grey field on Figure 4. It is clear that alkali loss has affected some of our least altered basalt samples and that the TAS diagram should be used with caution when classifying volcanic rocks.

Three of the Louisville Seamounts, Canopus (Site U1372), Rigil (Site U1374) and Burton (Site U1376), were drilled deep enough (232.9, 522.0 and 182.8 mbsf respectively) to look for changes of composition with depth. We use Nb/Zr plotted against depth (Fig. 3) to

assess this because Nb/Zr is sensitive to degree and depth of melting but insensitive to the effects of low-pressure fractional crystallisation. As can be seen in Figure 3 there is little systematic stratigraphic variation in Nb/Zr in the drill core from Rigil and Burton seamounts, but the volcanic rocks cored at Canopus (Site U1372) show three cycles of upward-decreasing Nb/Zr. This could be interpreted as showing cycles of increasing degree of mantle melting but with no obvious overall trend with time. The general lack of systematic compositional variation with depth in the IODP Expedition 330 drill holes was also noted by Nichols et al. (2014). Dorais et al. (2015) determined the rare-earth element (REE) concentrations in clinopyroxene phenocrysts in basalt from the IODP Expedition 330 drill core and used these to calculate the composition of the liquid from which they crystallised. In most cases these match the bulk composition of glasses analysed by Nichols et al. (2014) and indicate an alkaline parentage. The cores of some clinopyroxene phenocrysts from Rigil seamount, however, have distinct compositions suggesting that they originated as antecrysts derived from a transitional magma, but Dorais et al. (2015) found no evidence for the presence of tholeiitic magmas. If the Louisville seamounts have a tholeiitic basement then this must lie below the level sampled by the drill cores.

Incompatible element concentrations, normalised to primitive mantle (PM) values, for samples from the Louisville and Emperor seamounts are shown in Figure 5. Data from primitive olivine tholeiitic basalt (Kroenke-type basalt) from the Ontong Java Plateau (OJP) are shown for comparison. Several features are obvious on Figure 5. (1) The patterns for all five Louisville seamounts are remarkably similar to each other and to the post-shield basalt samples from the Emperor seamounts. (2) The Emperor shield lavas have similar patterns to those from the Louisville seamounts, but with more gentle negative slopes consistent with the former representing larger degrees of melting. (3) The Louisville seamounts show only a very weak trend towards overall enrichment with decreasing age from Canopus to Hadar. This

remarkable homogeneity has previously been noted among dredge samples from the LST by Beier et al. (2011) and Vanderkluisen et al. (2014). (4) The Louisville and Emperor patterns are virtually linear, with relative depletion in only the most incompatible elements. This feature is important because it implies that magmas in both seamount trails could have had a source resembling primitive (chondritic) mantle that had been only slightly depleted through the loss of a small melt fraction at some time in its history. (5) The Louisville and Emperor patterns are similar in shape to those for primitive OJP basalt, but are rotated about the least incompatible element (Lu) suggesting that the LST and HEST magmas could have been generated by variable but smaller-degree melting of a mantle source similar to the one that produced the OJP magmas. The nature of the LST mantle source and its partial melting will be discussed in the next section.

FORMATION OF THE LOUISVILLE AND EMPEROR MAGMAS

As was noted earlier, the LST and HEST have all the characteristics predicted for mantle plumes. The HEST is a product of a vigorous mantle plume and its output is increasing, in contrast to the LST whose output was always less vigorous (much smaller seamounts) and may well have ceased altogether in the last million years. Noble-gas isotopic studies on the LST (Hanyu, 2014) show that $^3\text{He}/^4\text{He}$ ranges up to 10.6 Ra, much lower than in basalt from Hawaii (up to ~ 30 Ra), but two LST basalt samples have a primordial Ne isotopic signature that implies a deep-mantle origin.

Both seamount chains have been active over a similar time interval (~ 80 – 0 Ma) in the Pacific Ocean. The age of the underlying ocean crust for each increases with decreasing seamount age (Fig. 2), and so both the LST and HEST seamounts were built on ocean lithosphere whose age, at the time of seamount formation, varied considerably over

approximately the same range (~15–80 Ma). Thus, the two sets of seamount data represent magmas formed from hotspots of varied vigour beneath lithosphere of widely varying thickness. If the relative vigour of the two hotspots is due largely to differences in mantle T_p , then the composition of their respective magmas should be predictable by a simple decompression-melting model.

The nature of the mantle source supplying magmas to Hawaii and other ocean islands has recently been the subject of considerable debate. Several authors have used the major element composition of basalts (e.g. Herzberg, 2011; Jackson et al., 2012) and the Ni content of their olivine phenocrysts (Sobolev et al., 2005) to argue that the source is at least partly composed of pyroxenite or eclogite rather than entirely peridotite. The return of oceanic crust to the mantle through subduction provides the source of this pyroxenite/eclogite. Other authors, however, have argued that pyroxenite/eclogite forms only a minor component of the mantle and that the composition of Hawaiian and other ocean island basalts can be explained adequately with a peridotite source. For example, Putirka et al. (2011) argued that the high Ni content of olivine phenocrysts in Hawaiian basalt results from high temperatures of crystallisation rather than from the olivine-free mantle source proposed by Sobolev et al. (2005). Putirka et al. (2011) also showed that partial melting experiments conducted on peridotite bulk compositions at pressures of 4–5 GPa can reproduce the range of composition of Hawaiian basalt. Rhodes (2015) showed that the isotopic diversity in basalt erupted over the magmatic history of Mauna Loa contrasts with a lack of major element variability, suggesting that there is no need for a major pyroxenite/eclogite component in the mantle source. There is less uncertainty in the composition of the mantle source of the LST magmas. Tejada et al. (2015) showed that basalt samples recovered during IODP Expedition 330 from Canopus, Rigil and Burton seamounts have remarkably constant initial $^{187}\text{Os}/^{188}\text{Os}$, with

values indistinguishable from that of primitive mantle and therefore precluding a significant recycled oceanic crust component in the LST mantle source.

In order to model the LST and HEST magma composition by decompression melting we consider two mantle compositions: pure peridotite and a 50:50 mixture of peridotite and pyroxenite/eclogite. The peridotite has a mineralogical composition given by McKenzie and O’Nions (1991): (1) 57.8% olivine, 27.0% orthopyroxene, 11.9% clinopyroxene and 3.3% spinel (spinel lherzolite); and (2) 59.8% olivine, 21.1% orthopyroxene, 7.6% clinopyroxene and 11.5% garnet (garnet lherzolite). Our mixed source consists of either spinel lherzolite mixed with pyroxenite (100% clinopyroxene), or garnet lherzolite mixed with eclogite (50% clinopyroxene, 50% garnet).

Magma composition is a function of mantle composition, the nature of the melting process, and degree and depth of partial melting. In order to model it we also need to know partition coefficients (D) between solid and liquid phases. For the present purposes we use a simple batch melting equation

$$C_L/C_0 = 1/(D+F-PF)$$

where C_0 is the initial concentration of some element in the mantle source, C_L is its concentrations in the liquid, F is the melt fraction, D is the average distribution coefficient for the mantle phases weighted by their respective mass fractions before the onset of melting, and P is the average distribution coefficient for the mantle phases weighted by their respective contribution to the melt. We use the following mantle melting proportions for spinel- and garnet lherzolite, respectively:

$$\text{liquid} = -0.22 \text{ ol} + 0.38 \text{ opx} + 0.71 \text{ cpx} + 0.13 \text{ sp} \quad (\text{Baker and Stolper, 1994})$$

$$\text{liquid} = 0.08 \text{ ol} - 0.19 \text{ opx} + 0.81 \text{ cpx} + 0.30 \text{ gt} \quad (\text{Walter, 1998}).$$

These values are used for both the peridotite source and the mixed source since they are determined by the composition of the primary magma, not the source. Partition coefficients (D) vary significantly with pressure, temperature and liquid composition, and this limits the reliability of partial melting models since the choice of values is always somewhat subjective. Here we have attempted to be more objective by using averages of all appropriate D values (Table 4).

It has been suggested that the LST and the 122 Ma Ontong Java Plateau (OJP) represent, respectively, the tail and head of the same mantle plume (e.g. Mahoney and Spencer, 1991). Basalt samples from the two have PM-normalised incompatible trace element patterns that are similar in shape (Fig. 5), implying that the LST magmas could have been produced by small-degree melting from a mantle source similar to that of the OJP magmas. The two also have similar initial $^{87}\text{Sr}/^{86}\text{Sr}$ and $^{143}\text{Nd}/^{144}\text{Nd}$ (Mahoney and Spencer, 1991; Vanderkluisen et al., 2014), and Tejada et al (2004) have shown that basalt samples from the OJP and Hawaii have near-identical Sr-, Nd-, Pb- and Hf-isotope ratios. The similarity in initial $^{87}\text{Sr}/^{86}\text{Sr}$ and ϵNd between basalt samples from the LST, Hawaii and OJP (Fig. 6) suggests that these have compositionally similar mantle sources. Data from the other Hawaiian islands and the HEST, however, show a much larger range indicating considerable heterogeneity in the Hawaiian plume (e.g. Huang et al., 2013; Harrison et al., 2020). The array of HEST data extending towards the composition of East Pacific Rise basalt (Fig. 6) suggests either mixing with ambient upper mantle or the presence of a depleted, refractory plume component that is only sampled by large degrees of melting when the plume was situated close to a mid-ocean ridge (Regelous et al., 2004). Recent work by Harrison et al. (2020) has shown that the HEST has sampled both ambient upper mantle and a depleted plume component in variable proportions over time. Despite heterogeneity in the HEST mantle source, the isotopic similarity of basalt from the OJP, LST, Hawaii and some of the

HEST (Fig. 6) suggests that these have similar mantle sources. It should therefore be possible to model their incompatible-element abundances using a common mantle source based on the composition of primitive OJP basalt. We use this approach to calculate the composition of the peridotite mantle source. The pyroxenite and eclogite components of our mixed source are assumed to have the incompatible element abundances of average normal mid-ocean ridge basalt given by Sun and McDonough (1989).

Calculating the composition of the OJP mantle source is straightforward because primitive (Kroenke-type) basalt, containing sparse microphenocrysts of olivine and Cr-spinel, was recovered from the OJP during ODP Leg 192 (Mahoney et al., 2001). Using forward and inverse mantle-melting modelling, Herzberg (2004) showed that these basalts were produced by around 30% melting, and Fitton and Godard (2004) obtained the same value using incompatible trace element concentrations measured on the same samples. Tejada et al. (2004) showed that the isotopic characteristics of OJP basalts can be explained by removing ~1% by mass of a small melt fraction (e.g. continental crust) from primitive mantle at about 3 Ga, a process that can also account for the incompatible element composition of Kroenke-type basalt (Fitton and Godard, 2004). In the present study we calculate the peridotite mantle composition from that of Kroenke-type basalt. First, we calculate the composition of the primary magma by incrementally adding equilibrium olivine to the composition of six unaltered samples of Kroenke-type basalt from ODP Sites 1185 and 1187 until the olivine composition reached Fo_{91.6} (Herzberg, 2004). The amount of olivine added ranges from 29.6 to 33.4 wt.% and the calculated primary magmas contain 18.9 to 19.4 wt.% MgO. We then calculate the composition of the OJP mantle source by assuming that the primary magmas were produced by 30% melting, leaving a harzburgite residue composed of 75% olivine and 25% orthopyroxene. The composition of the mantle source was calculated by mass balance:

$$C_0 = C_L(D'+F-D'F)$$

where C_L is the average primary magma composition and D' is the bulk D of the residual harzburgite, calculated from the D values given in Table 4. Since $D \approx 0$ for incompatible elements in olivine and orthopyroxene, $C_0 \approx 0.3C_L$ for 30% melting. The calculated mantle composition and further details of the calculations are given in Hastie et al. (2016).

The results of modelling rare-earth element (REE) ratios in the Louisville and Emperor data are shown in Figure 7. The LST data define a trend in which decreasing degree of partial melting (~ 3 to $\sim 1.5\%$) is accompanied by increasing proportion of garnet (30 to 100%) in the case of the peridotite mantle source (Fig. 7a). A mixed peridotite+pyroxenite/eclogite mantle source (Fig. 7b) can also reproduce the REE ratios, but with larger implied melt fractions. The younger seamounts (Achernar and Hadar) appear to have been formed by smaller degrees of melting than do the older seamounts (Canopus, Rigil and Burton). Data from the HEST generally indicate higher degrees of melting (~ 2 to $\sim 10\%$) of a spinel- to garnet lherzolite source. Although it is common practice to use the batch melting equation to model geochemical data, melting accompanied by melt segregation is a dynamic process that lies between batch and fractional melting. Consequently, the melt fractions implied by the model curves in Figure 7 can only give an approximation to reality. However, the use of the batch melting equation is justified here because the results of batch and fractional melting converge as melt fraction (F) tends to zero, and the relative variation in depth and melt fraction will be robust. We use a more sophisticated incremental melting model later to assess the effects of lithosphere thickness on melt composition.

An attempt to model the concentrations of Nb and Zr in the LST and HEST data is shown in Figure 8. The LST data define an array that extrapolates to the origin suggesting that it is mostly controlled by low-pressure fractional crystallisation of phases (olivine, plagioclase

and augite) containing low concentrations of Nb and Zr, but it is clear that the younger seamounts have slightly higher Nb/Zr than the older seamounts. The modelling results for a peridotite source (Fig. 8a) are broadly consistent with the degrees of melting implied by the rare-earth element ratios (Fig. 7a), but the attempt to model Zr and Nb concentrations using a mixed source (Fig. 8b) failed to account for the LST data because of the high Zr and Nb contents of the pyroxenite component. Taken together, Figures 7 and 8 show clearly that the HEST was formed by generally higher degrees of melting of a peridotite mantle source containing smaller proportions of garnet than were the LST. It is possible that the HEST and LST formed from mantle sources with significantly different compositions rather than from the common OJP source that we assume here, but the generally similar isotopic composition of Louisville, Hawaiian and OJP basalts (Fig. 6; Mahoney and Spencer, 1991, Tejada et al., 2004, 2015; Vanderkluysen et al., 2014) makes this unlikely. Since the lithosphere age, and therefore thickness, at the time of seamount formation varied over the same range for the LST and HEST (Figs. 1 and 2), the differences in degree of melting and mantle mineralogy between the two trails is most likely due to differences in the T_p of their respective sources. This hypothesis is tested in the next section.

VARIATION OF MAGMA COMPOSITION WITH LITHOSPHERE THICKNESS

Decompression melting in mantle plumes is controlled mostly by T_p and lithosphere thickness. The depth at which melting starts increases with increasing T_p , and degree of melting increases steadily with falling pressure until upwelling and decompression are stopped by the lithosphere lid. A simple model of decompression melting in mantle plumes is shown in Figure 9. In this model melting starts on the dry mantle solidus ($F=0$) and reaches a maximum (F_{\max}) at the base of the lithosphere. Increasing lithosphere thickness suppresses

melting such that no melt can form in volatile-free mantle with $T_p=1300^\circ\text{C}$ when lithosphere thickness exceeds 57 km, whereas it would take a lithosphere thickness of ~ 120 km to prevent melting of mantle with $T_p=1500^\circ\text{C}$ (Fig. 9). The rate at which melt is produced with falling pressure above the mantle solidus is governed by the latent heat of fusion. Here we use a value of 1.2%/kbar (0.4%/km), which is the value proposed by Klein and Langmuir (1987) and is within the range of values calculated by McKenzie and Bickle (1988). We use the same value for both our peridotite and mixed mantle sources because it relates mostly to the conversion of excess temperature above the solidus to the latent heat of fusion of clinopyroxene and garnet to produce basaltic melt. The rate of melt production should therefore be insensitive to the proportion of olivine and orthopyroxene in the source. We also assume that the garnet-spinel transition is the same in both our peridotite and mixed mantle sources. In the absence of volatiles, melts from mantle with $T_p < 1350^\circ\text{C}$ will form entirely from spinel-lherzolite whereas hotter mantle will melt initially in the garnet-lherzolite stability field. The addition of small amounts of volatiles (H_2O or CO_2) to the mantle will result in the formation of small amounts of melt at greater depth (Fig. 9), with the amount of melt limited by the volatile content and its solubility in the melt.

We can use the model in Figure 9 to calculate the chemical composition of magmas from the mantle T_p and the lithosphere thickness. To do this we assume that the melt is the aggregate of all partial melts in a column of mantle extending from the depth to the mantle solidus ($F=0$) to the base of the lithosphere ($F=F_{\text{max}}$). We use Nb/Zr and Ce/Y to illustrate the effect of T_p and lithosphere thickness on melt composition (Fig. 10). These ratios are useful because they represent the whole range of incompatible elements (Fig. 5) and are unaffected by low-temperature alteration or low-pressure fractional crystallisation, but both are sensitive to the presence of garnet in the source. We calculate Nb/Zr and Ce/Y in the aggregate melt by calculating the composition of individual contributions to the melt in 1-km steps (0.4%

increments) through the thickness of the mantle column from the solidus to the base of the lithosphere (Fig. 9). The aggregate melt composition is the average of all the individual melts weighted by their mass fraction. The procedures and parameters used are as described in the previous section. Figure 10 shows that Nb/Zr and Ce/Y in the aggregate melt are relatively insensitive to mantle source composition, especially in the case of Nb/Zr where the peridotite and mixed source curves are virtually identical. This is not surprising given that our two mantle sources differ only in the modal abundance (but only slightly in relative proportion) of clinopyroxene and garnet, and it is these phases that contribute most to the melt.

To compare our analytical data with the model curves in Figure 10 requires that we know the thickness of the lithosphere beneath each seamount at the time the seamount formed. The age of the lithosphere at the time of an individual seamount's formation is the difference between the age of the seamount and the age of the seafloor on which it grew, and this can easily be found from the age data in Figure 2. Converting lithosphere age into lithosphere thickness is much less straightforward, largely because of uncertainties in the appropriate definition of thickness. To what depth can mantle plumes rise before further upwelling is inhibited by a rigid lid? Olson et al. (1988) have shown that thermal plumes do not effectively intrude and erode the lithosphere in a moving plate, so we can use steady-state lithosphere thicknesses. Here we choose the 1100°C isotherm as the likely base of the rigid lithosphere, as found by Watson and McKenzie (1991) in their modelling of melting in the Hawaiian plume, and we use the plate model of McKenzie et al. (2005) to relate lithosphere age to the depth of this isotherm. Lithosphere thickness at the time of eruption of individual seamounts within the LST and HEST were estimated and plotted with Nb/Zr and Ce/Y data on Figure 10. Data for the shield-forming lavas of Mauna Kea, sampled by the Hawaii Scientific Drilling Project (Rhodes and Vollinger, 2004), are included for comparison. Adjustments were made to the data for the HEST (from Regelous et al., 2003; Huang et al.,

2005) and Hawaii to allow for small differences in the values reported for USGS reference standard BHVO-2 from those we obtained when analysing the LST samples (Table 2).

The model curves on Figure 10 fit the HEST and Hawaii data remarkably well considering uncertainties in lithosphere thickness and the assumptions we made in our melting calculations. The low-Nb/Zr, low-Ce/Y HEST samples, including those from Hawaii, are all from the shield-forming stages of their respective volcanoes, and these can be explained by decompression melting of mantle with $T_p=1500^\circ\text{C}$. This temperature is similar to that for the centre of the Hawaiian plume obtained through numerical modelling (Watson and McKenzie, 1991) and from Fe-Mg relationships in Hawaiian picrite (Herzberg et al., 2007). Samples with higher Nb/Zr and Ce/Y represent the post-shield stage (Regelous et al., 2003) and data from these plot between the curves for $T_p=1300$ and 1400°C , implying that they formed from the cooler sheath around the plume as the seamount drifted away from the plume axis. Thus, the HEST and Hawaii data can be explained adequately by decompression melting in a mantle plume.

The Louisville data show a slight increase in Nb/Zr and Ce/Y, implying a small decrease in degree of melting, with increasing lithosphere thickness but the variations in Nb/Zr and Ce/Y are far less than predicted by the model (Fig. 10). Adjusting the input parameters (mantle mineralogy, D values, depth to the spinel-garnet transition, and latent heat of fusion) of our model would change the position of the curves but not their form and would therefore not improve the fit to the LST data. The composition of the two oldest Louisville seamounts (Canopus and Rigil) is particularly difficult to explain by simple decompression melting because they were apparently formed on young lithosphere that was only 35–45 km thick. Figure 10 shows that a mantle plume with $T_p>1300^\circ\text{C}$ impinging on such thin lithosphere ought to melt far more than the 1.5–3% implied by the composition of basalt from

these two seamounts (Figs. 7 and 8) and produce tholeiitic magmas with much lower Nb/Zr than is observed. It is, of course, possible that such rocks exist at depths beyond the range of drilling, but drilling at Site U1374 on Rigel Seamount penetrated about 15% of the distance to the base of the seamount (a minimum value because some material would have been removed by erosion) without any systematic change in basalt composition (Fig. 3). Shield-forming tholeiite forms >95% of the volume of Hawaiian volcanoes (Clague, 1987). Possible reasons for the misfit between the predicted and observed composition of the Louisville seamounts are discussed in the next section.

ORIGIN OF THE LOUISVILLE SEAMOUNTS

Our decompression-melting model can explain the compositional variation of the HEST very well and yet appears unable to account for the relatively constant composition of the LST. One possible reason for this could be that the seafloor ages that we have used, and hence the estimated lithosphere thicknesses, are in error. The seafloor beneath the north-westerly part of the LST formed during the Cretaceous normal superchron (121–83 Ma; Cande and Kent, 1995) and so its age is unconstrained by magnetic anomalies. Consequently, the seafloor ages given in Figure 2 were based on inferred ages for the initiation and cessation of spreading on the Osborn Trough. The age of its initiation is based on the assumption that the Early Cretaceous Manihiki and Hikurangi Plateaus originally formed part of the Greater Ontong Java Plateau and were rifted apart by spreading on the Osborn Trough. Its demise is dated through the tentative identification of magnetic anomalies 33 and 32 around the trough (Billen and Stock, 2000; Worthington et al., 2006; Downey et al., 2007). It is possible that spreading on the Osborn Trough ceased much later than 86 Ma, but this would require higher spreading rates. Billen and Stock (2000) estimate that a full spreading rate of 20 cm/yr

would be required if spreading ceased at 105 Ma. The relative constancy in the composition of the seamounts would require that they were all emplaced on lithosphere of similar thickness if the magmas were generated by simple decompression melting to the base of the lithosphere. This would require a lithosphere age of at least 75 Ma (e.g. McKenzie et al., 2005) and therefore a present-day age of ~150 Ma for the ocean crust beneath Canopus Seamount, an age that falls a long way outside all current estimates and would therefore require a radical reassessment of the history of the western Pacific Ocean. We must conclude that the lithosphere ages given in Figure 2 are at least approximately correct and therefore find an alternative explanation for the misfit.

Seamounts on the HEST are generally much larger than those on the LST implying a much higher rate of magma production in the former. As noted earlier, King and Adam (2014) estimate that the HEST mantle buoyancy flux is nearly an order of magnitude higher than that for the LST. If the two seamount trails formed on seafloor with the same range of ages (Fig. 2) then the lithosphere beneath the two has the same range of thickness. The greater magma productivity in the HEST must, therefore, imply a higher T_p in the Hawaiian hotspot than in that responsible for the LST. Nichols et al. (2014) have used the volatile content of glassy margins of intrusive sheets in Burton and Hadar to estimate depth of emplacement and hence the uplift and subsequent subsidence history of the two seamounts. They show that these can be explained by a thermal anomaly beneath the Louisville seamounts that is no more than 100°C hotter than normal upper mantle temperature, implying a T_p of 1300–1400°C beneath these seamounts. This is at least 100°C cooler than our estimate for the temperature of the mantle beneath the Emperor seamounts. Attempts to verify this independently with PRIMELT3 (Herzberg and Asimow, 2015) failed because even the most primitive LST magmas, represented by basalt samples with $Mg\# > 70$, had crystallised clinopyroxene as well as olivine.

We show that mantle with $T_p=1350\text{--}1400^\circ\text{C}$ decompressing to depths as shallow as 40–50 km should melt to a much larger extent than the 1.5–3% implied by our data (Fig. 10). Furthermore, mantle with $T_p\leq 1350^\circ\text{C}$ would melt entirely within the spinel lherzolite stability field (Fig. 9), whereas the composition of our LST samples requires that a large proportion of the magma formed from garnet lherzolite (Figs. 7 and 8). Earlier we posed the question: to what depth can mantle plumes rise before further upwelling is inhibited by a rigid lid? The answer in the case of the Louisville seamounts is clearly not at the base of the lithosphere as defined by plate models (e.g. McKenzie et al., 2005). We need a mechanism for generating small-degree melt, largely in the garnet lherzolite stability field, and then preventing further melting irrespective of lithosphere thickness. Melting in the presence of a small amount of volatile components (H_2O or CO_2) could provide one. The addition of as little of 0.05% of water to the mantle increases the depth of onset of melting by ~ 45 km (Katz et al., 2003; Fig. 9). This value is similar to that determined by Sarafian et al. (2017) who show that the addition of 0.045% of water increases the depth of onset of mantle melting by 34 km. The amount of melt produced at depths greater than that of the dry solidus would be limited by the concentration of volatile components in the mantle and their solubility in the melt.

The presence of water has been shown to lower peridotite viscosity by 2–3 orders of magnitude relative to anhydrous peridotite (Hirth and Kohlstedt, 1996). Ito et al. (1999) show that dehydration of the mantle through partial melting results in a 50-fold increase in its viscosity, which they argue is enough to restrict further upwelling of a hot ($T_p=1530^\circ\text{C}$) mantle plume beneath a mid-ocean ridge, as in Iceland. Hirth and Kohlstedt (1999) calculate that 125 ppm of water in the mantle beneath mid-ocean ridges would result in 1–2% melting between the wet and dry solidi. Thus it seems likely that the production of a small amount of volatile-rich melt in a relatively cool mantle plume ($T_p=1350\text{--}1400^\circ\text{C}$), such as that responsible for the LST, would increase the viscosity of the residual mantle and prevent it

from reaching the dry mantle solidus and melting further. A mantle plume with $T_p=1350^\circ\text{C}$ would start to melt at a depth of ~ 120 km (Fig. 9) and produce a small amount of melt in the garnet lherzolite stability field. Further ascent and decompression would be limited by increasing viscosity, and this could prevent it from reaching the dry mantle solidus and the garnet/spinel boundary at ~ 70 km. Varying the lithosphere thickness between 35 and 60 km, as in the case of Canopus, Rigil and Burton seamounts (Fig. 10), would have little if any effect on magma composition. The very slight reduction of melt fraction with decreasing age apparent in the LST data (Figs. 7, 8 and 10) could reflect a very reduced influence of lithosphere thickness or could be due to a small reduction of T_p . A hotter mantle plume ($T_p\approx 1500^\circ\text{C}$) beneath the HEST would have lower viscosity before the onset of melting, melt to a larger extent, and decompress to the base of the lithosphere as in the model in Figures 9 and 10. The initial 1–2% of melt produced by dehydration melting of garnet lherzolite would be diluted by much larger degrees of melting of spinel lherzolite. In this way our simple decompression melting model can account for the composition of both the HEST and LST.

COMPARISON WITH OTHER OCEAN-ISLAND BASALTS

The lack of variation in the composition of the LST with lithosphere age and thickness raises the question of whether the same is true of ocean-island basalt (OIB) in general. Figure 11 shows the variation of Nb/Zr and Ce/Y with lithosphere age in a large OIB data set (from Fitton, 2007). The data show no correlation between Nb/Zr and lithosphere age and only a very weak correlation for Ce/Y. Islands formed on the oldest lithosphere (e.g. the Canary, Comores and Caroline Islands) have a similar range of composition to those formed close to spreading centres (e.g. Ascension, Azores and Rodrigues). This appears to contradict Ellam (1992) who showed that the average Ce/Y values for individual islands varies with

lithosphere age and therefore thickness, but this discrepancy is due largely to the much larger data set used in the present study. Ellam's (1992) correlation between lithosphere age and Ce/Y in OIB defined a convex-upwards data array, whereas a true relationship would produce a convex-downward array (Fig. 11). In a more recent study, Niu et al. (2011) averaged a large set of OIB data in 10 km lithosphere thickness intervals and showed linear variations of several geochemical parameters (notably REE ratios) with lithosphere thickness. The data averages show a twofold increase in Sm/Yb as lithosphere thickness increases from 0 to 90 km, and they ascribe this to a progressive increase in depth and decrease in degree of melting ("the lid effect"). Our data show a similar increase in Ce/Y between the Ascension and Canaries data (Fig. 11) although the data scatter obscure any linear trend. However, our melting model predicts a much greater dependence on lithosphere thickness for ratios such as Ce/Y and Sm/Yb that are sensitive to the abundance of garnet in the mantle (Figs. 10 and 11). Decompression melting of volatile-free peridotite is, therefore, incapable of accounting for the composition of most OIB and its weak dependence on lithosphere thickness (Fig. 11).

Basalt from Iceland, the Galapagos Islands, and the shield-forming stage of the Hawaiian Islands and Emperor seamounts have lower Nb/Zr and Ce/Y than other OIB (Fig. 11), implying larger degrees of melting consistent with our melting model. These basalts are tholeiitic, in contrast to the alkaline basalt forming most ocean islands and, along with basalt from Samoa (also with low Nb/Zr), have the highest $^3\text{He}/^4\text{He}$ measured in OIB (Class and Goldstein, 2005). These islands are clearly different from other ocean islands and are the products of vigorous mantle plumes decompressing under lithosphere of varying thickness. Iceland and the Galapagos Islands are located on or close to spreading centres, whereas the Hawaiian Islands are located on lithosphere that is ~90 Ma old. The Hawaiian Islands are probably unique among ocean islands in being largely composed of tholeiitic shield-forming basalt that formed by melting beneath thick lithosphere. This requires large degrees of mantle

melting within the hottest mantle plume observed on Earth today (Watson and McKenzie, 1991; Herzberg et al., 2007).

Other ocean islands are most likely the product either of less vigorous mantle plumes that lack the buoyancy to overcome the stalling effect of dehydration melting or are not the product of mantle plumes at all. Some intraplate volcanic provinces, including ocean islands, are demonstrably not related to plume activity (e.g. Guimarães et al., 2020), and this may also be true of the majority of ocean islands. The wide compositional range of OIB magmas generated beneath lithosphere of all thicknesses requires a heterogeneous mantle source (e.g. Dasgupta et al., 2010). These authors showed that the major-element composition of OIB can be explained with a source composed of peridotite mixed with discrete bodies of carbonated eclogite and a silica-oversaturated eclogite. The more easily fusible character of these bodies removes the need for mantle plumes in the majority of ocean islands, which may be formed instead by decompression melting of enriched components within the general upper mantle convective flow.

CONCLUSIONS

Drilling during IODP Expedition 330 provided volcanic rock samples from five of the Louisville seamounts, and three of the holes penetrated deep enough to have sampled rocks from the shield-forming phase of seamount growth. Geochemical data on the rock samples confirm the conclusion from earlier dredging expeditions that the Louisville seamounts are mostly composed of alkali basalt with a remarkably uniform composition.

The composition of the Louisville basalt samples can be modelled by ~1.5–3% melting of garnet lherzolite with only a small contribution from spinel lherzolite. By contrast,

the composition of basalt from the Emperor seamounts requires larger degrees of melting (2–10%) and mantle sources ranging from spinel- to garnet lherzolite. A mantle source composition calculated from the composition of primitive tholeiitic basalt from the Ontong Java Plateau (Hastie et al., 2016) was used in all melting calculations.

Decompression melting in a mantle plume impinging on the base of the lithosphere ought to produce magmas whose composition is determined by mantle T_p and lithosphere thickness. The ages of the Louisville and Emperor seamounts and of their underlying ocean crust are known, and so the age of the lithosphere at the time of seamount formation can be calculated by subtracting the former from the latter. This is then used to estimate lithosphere thickness from the plate model of McKenzie et al. (2005). Both seamount trails formed on lithosphere with the same range of lithosphere thickness (~35–85 km). The composition of the accumulated melt produced by decompression melting in a column of mantle extending from the mantle solidus to the base the lithosphere is calculated for $T_p=1300, 1400$ and 1500°C and compared with the composition of basalt from the Emperor and Louisville seamounts. The composition of basalt from the tholeiitic shield-forming phase of the Emperor seamounts and Hawaii compares well with that predicted for mantle with $T_p=1500^\circ\text{C}$ while the composition of post-shield alkali basalt fits the prediction for $T_p=1300\text{--}1400^\circ\text{C}$. This is consistent with the generation of the early, shield-forming magmas in the core of a mantle plume and the later, post-shield magmas in the cooler plume sheath as the seamount drifts away from the plume axis. Differences between shield and post-shield basalt in radiogenic isotope ratios (e.g. Hanano et al., 2010) and ΔNb (the relative enrichment in Nb on a plot of Nb/Y against Zr/Y; Fitton, 2007; Greene et al., 2010, Harrison et al., 2020) limit the reliability of modelling the two with a common mantle source. However, this is unlikely to affect the conclusion that post-shield magmas were produced by smaller degrees of melting of cooler mantle.

Basalt from the Louisville seamounts is remarkably uniform in composition even though lithospheric thickness at the time of seamount formation varied considerably. Such homogeneity is not predicted by our decompression melting model but the problem can be resolved if the Louisville seamounts were formed by dehydration melting of mantle containing a small amount of volatiles in a cooler plume. Hydrous melting in a relatively cool mantle plume ($T_p=1350\text{--}1400^\circ\text{C}$) could produce a small amount of melt and then be inhibited by increasing viscosity from reaching the dry mantle solidus and melting further. The failure of the plume to reach the dry mantle solidus or the base of the lithosphere means that the resulting magmas would have the same composition irrespective of lithosphere thickness. This lack of influence of lithospheric thickness on basalt composition is a general feature of most ocean islands. Only a few ocean islands (e.g. Iceland, Galapagos and the Hawaiian Islands) are composed of tholeiitic basalt whose composition can potentially be explained by dry decompression melting of a peridotite mantle source beneath lithosphere of the respective thickness. The Hawaiian Islands are unique in being composed dominantly of tholeiitic basalt formed by decompression melting beneath thick lithosphere, and this requires an exceptionally hot mantle plume. A mantle plume with $T_p\approx 1500^\circ\text{C}$ beneath the Emperor Seamounts and Hawaiian Islands would have lower viscosity before the onset of melting, melt to a larger extent, and decompress to the base of the lithosphere. Thus, our simple decompression melting model could explain the composition of both the Emperor and Louisville seamounts, but probably not ocean islands in general. Most islands may not be the product of mantle plumes but instead be formed by decompression melting of heterogeneous mantle within the general upper mantle convective flow.

ACKNOWLEDGEMENTS

This research used samples provided by the Integrated Ocean Discovery Program (IODP). Funding was provided by the UK Natural Environment Research Council through grants to JGF (grant number NE/1022205/1) and ADS (grant number NE/J005401/1). We are grateful to Nic Odling and Sam Hammond for assistance with XRF and ICP-MS analyses, respectively, and to Fred Frey, Mike Garcia, Keith Putirka, Cin-Ty Lee and Shichun Huang for their constructive criticism of this paper.

REFERENCES

- Baker, M.B. and Stolper, E.M. (1994) Determining the composition of high-pressure mantle melts using diamond aggregates. *Geochimica et Cosmochimica Acta* 58, 2811–2827.
- Ballance, P. F., Scholl, D. W., Vallier, T. L., Stevenson, A. J., Ryan, H. and Herzer, R. H. (1989). Subduction of a Late Cretaceous Seamount of the Louisville Ridge at the Tonga Trench: A model of normal and accelerated tectonic erosion. *Tectonics* 8, 953–962.
- Beier, C., Vanderkluysen, L., Regelous, M., Mahoney, J. J. and Garbe-Schönberg, D. (2011). Lithospheric control on geochemical composition along the Louisville Seamount Chain. *Geochemistry Geophysics Geosystems* 12, Q0AM01, doi:10.1029/2011GC003690.
- Billen, M. and Stock, J. (2000). Morphology and origin of the Osbourn Trough. *Journal of Geophysical Research* 105, 481–489.
- Buchs, D.M., Williams, R. Sano, S. and Wright, V.P. (2018). Non-Hawaiian lithostratigraphy of Louisville seamounts and the formation of high-latitude oceanic islands and guyots. *Journal of Volcanology and Geothermal Research* 356, 1–23.
- Cande, S.C. and Kent, D.V. (1995). Revised calibration of the geomagnetic polarity timescale for the Late Cretaceous and Cenozoic. *Journal of Geophysical Research* 100, 6093–6095.

- Cheng, Q., Park, K.-H., Macdougall, J.D., Zindler, A., Lugmair, G.W., Staudigel, H., Hawkins, J. and Lonsdale, P. (1987) Isotopic Evidence for a Hotspot Origin of the Louisville Seamount Chain, in *Seamounts, Islands, and Atolls* (eds B. H. Keating, P. Fryer, R. Batiza and G. W. Boehlert), American Geophysical Union, Washington, D. C., 283–296.
- Clague, D.A. (1987). Hawaiian alkaline volcanism. In Fitton, J.G and Upton, B.G.J. (Eds.), *Alkaline Igneous Rocks*. Geological Society Special Publication 30, 227–252.
- Class, C. and Goldstein, S.L. (2005). Evolution of helium isotopes in the Earth's mantle. *Nature* 436, 1107–1112.
- Dasgupta, R., Jackson, M.G. and Lee, C-T.A. (2010). Major element chemistry of ocean island basalts — Conditions of mantle melting and heterogeneity of mantle source. *Earth and Planetary Science Letters* 289, 377–392.
- Dorais, M. J. (2015). Exploring the mineralogical heterogeneities of the Louisville Seamount Trail, *Geochemistry Geophysics Geosystems*, 16, 2884–2899, doi:10.1002/2015GC005917.
- Dorais, M.J. and Buchs (2019). Mineralogical characterization of rejuvenated magmatism at Burton Guyot, Louisville Seamount trail. *Contributions to Mineralogy and Petrology* 174, 66.
- Downey, N. J., Stock, J. M., Clayton, R. W. and Cande, S. C. (2007). History of the Cretaceous Osborn spreading center. *Journal of Geophysical Research* 112, B04102.
- Elkins, L.J., Gaetani, G.A. and Sims, K.W.W. (2008). Partitioning of U and Th during garnet pyroxenite partial melting: Constraints on the source of alkaline ocean island basalts. *Earth and Planetary Science Letters* 265, 270–286.
- Ellam, R.M. (1992). Lithospheric thickness as a control on basalt geochemistry. *Geology* 20, 153–156.

Fitton, J.G. (2007). The OIB paradox. In: Foulger, G.R. and Jurdy, D.M. (eds.) *Plates, Plumes, and Planetary Processes*, Geological Society of America Special Paper 430, 387–412.

Fitton, J.G. and Godard M., (2004). Origin and evolution of magmas on the Ontong Java Plateau. In Fitton, J.G., Mahoney, J.J., Wallace, P.J. and Saunders, A.D. (Eds.), *Origin and Evolution of the Ontong Java Plateau*. Geological Society Special Publication 229, 151–178.

Fitton, J.G., Saunders, A.D. Larsen, L.M., Hardarson, B.S. and Norry, M.J. (1998). Volcanic rocks from the southeast Greenland margin at 63°N: composition, petrogenesis and mantle sources. *Proceedings of the Ocean Drilling Program, Scientific Results* 152, 331–350.

Greene, A. R., Garcia, M.O., Weis, D., Ito, G., Kuga, M., Robinson, J. and Yamasaki, S. (2010). Low-productivity Hawaiian volcanism between Kaua‘i and O‘ahu, *Geochemistry Geophysics Geosystems*, 11, Q0AC08, doi:10.1029/2010GC003233.

Guimarães, A.R., Fitton, J.G., Kirstein, L.A. and Barfod, D.N. (2020). Contemporaneous intraplate magmatism on conjugate South Atlantic margins: A hotspot conundrum. *Earth and Planetary Science Letters* 536, 116147.

Hanano, D., Weis, D., Scoates, J.S. Aciego, S. and DePaolo, D.J. (2010). Horizontal and vertical zoning of heterogeneities in the Hawaiian mantle plume from the geochemistry of consecutive postshield volcano pairs: Kohala-Mahukona and Mauna Kea–Hualalai. *Geochemistry Geophysics Geosystems*, 11, Q01004, doi:10.1029/2009GC002782.

Hanyu, T. (2014). Deep plume origin of the Louisville hotspot: noble gas evidence. *Geochemistry Geophysics Geosystems* 15, 565–576, doi:10.1002/2013GC005085.

- Harrison, L.N., Weis, D., and Garcia, M.O. (2020). The multiple depleted mantle components in the Hawaiian-Emperor chain. *Chemical Geology* 532, doi: 10.1016/j.chemgeo.2019.119324.
- Hart, S.R. and Dunn, T. (1993). Experimental cpx/melt partitioning of 24 trace elements. *Contributions to Mineralogy and Petrology* 113, 1–8.
- Hastie, A.R., Fitton, J.G., Kerr, A.C., McDonald, I., Schwindrofska, A. and Hoernle, K. (2016). The composition of mantle plumes and the deep Earth. *Earth and Planetary Science Letters* 444, 13–25.
- Hauri, E.H., Wagner, T.P. and Grove, T.L. (1994). Experimental and natural partitioning of Th, U, Pb and other trace elements between garnet, clinopyroxene and basaltic melts. *Chemical Geology* 117, 149–166.
- Hawkins, J.W., Lonsdale, P.F. and Batiza, R. (1987). Petrologic Evolution of the Louisville Seamount Chain, in *Seamounts, Islands, and Atolls* (eds B. H. Keating, P. Fryer, R. Batiza and G. W. Boehlert), American Geophysical Union, Washington, D. C., 235–254.
- Herzberg, C. (2004). Partial melting below the Ontong Java Plateau. In Fitton, J.G., Mahoney, J.J., Wallace, P.J. and Saunders, A.D. (Eds.), *Origin and Evolution of the Ontong Java Plateau*. Geological Society Special Publication 229, 179–184.
- Herzberg, C. (2011). Identification of Source Lithology in the Hawaiian and Canary Islands: Implications for Origins. *Journal of Petrology* 52 113–146.
- Herzberg, C. and Asimow, P.D. (2015). PRIMELT3 MEGA.XLSM software for primary magma calculation: Peridotite primary magma MgO contents from the liquidus to the solidus. *Geochemistry, Geophysics, Geosystems* 16: 563–578. Doi:10.1002/2014GC005631.

Herzberg, C., Asimow, P.D., Arndt, N., Niu, Y., Leshner, C.M., Albarède, F., Fitton, J.G., Cheadle, M.J. and Saunders, A.D. (2007). Temperatures in ambient mantle and plumes: constraints from basalts, picrites and komatiites. *Geochemistry Geophysics Geosystems* 8, Q02006, doi:10.1029/2006GC001390.

Hirth, G. and Kohlstedt, D.L. (1996). Water in the oceanic upper mantle: implications for rheology, melt extraction, and the evolution of the lithosphere. *Earth and Planetary Science Letters* 144, 93–108.

Horn, I., Foley, S.F., Jackson, S.E. and Jenner, G.A. (1994). Experimentally determined partitioning of high field strength- and selected transition elements between spinel and basaltic melt. *Chemical Geology* 117, 193–218.

Huang, S., Regelous, M., Thordarson, T and Frey, F.A. (2005). Petrogenesis of lavas from the Detroit Seamount: geochemical differences between Emperor Chain and Hawaiian volcanoes. *Geochemistry, Geophysics, Geosystems* 6, Q01L06, doi: 10.1029/2004GC000756.

Huang, S., Blichert-Toft, J., Fodor, R.V., Bauer, G.R. and Bizimis, M. (2013). Sr, Nd, Hf and Pb isotope systematics of postshield-stage lavas at Kahoolawe, Hawaii. *Chemical Geology* 360–361, 159–172.

Irving, A.J. (1978). A review of experimental studies of crystal/liquid trace element partitioning. *Geochimica et Cosmochimica Acta* 43, 754–770.

Ito, G., Shen, Y., Hirth, G. and Wolfe, C.J. (1999). Mantle flow, melting, and dehydration of the Iceland mantle plume. *Earth and Planetary Science Letters* 165, 81–96.

Jackson, M. G., Weis, D. and Huang, S. (2012). Major element variations in Hawaiian shield lavas: Source features and perspectives from global ocean island basalt (OIB) systematics, *Geochemistry, Geophysics, Geosystems* 13, Q09009, doi:10.1029/2012GC004268.

- Johnson, K.T.M. (1998). Experimental determination of partition coefficients for rare earth and high-field-strength elements between clinopyroxene, garnet, and basaltic melt at high pressures. *Contributions to Mineralogy and Petrology* 133, 60–68.
- Katz, R.F., Spiegelman, M. and Langmuir, C.H. (2003). A new parameterization of hydrous mantle melting, *Geochemistry Geophysics Geosystems* 4(9), 1073, doi:10.1029/2002GC000433, 2003.
- King, S.C. and Adam, C. (2014). Hotspot swells revisited. *Physics of the Earth and Planetary Interiors* 235, 66–83.
- Klein E.M., Langmuir C.H. (1987). Global correlations of ocean ridge basalt chemistry with axial depth and crustal thickness. *Journal of Geophysical Research* 92, 8089–8115.
- Klemme, S. and O'Neill, H.StC. (2000). The near-solidus transition from garnet lherzolite to spinel lherzolite. *Contributions to Mineralogy and Petrology* 138, 237–248.
- Koppers, A. A. P., Duncan, R. A. and Steinberger, B. (2004). Implications of a nonlinear 40 Ar/ 39 Ar age progression along the Louisville seamount trail for models of fixed and moving hot spots. *Geochemistry Geophysics Geosystems* 5, Q06L02, doi:10.1029/2003GC000671.
- Koppers, A.A.P., Yamazaki, T., Geldmacher, J, Gee, J.S., Hoshi, H. et al. (2012a). Limited latitudinal mantle plume motion for the Louisville hotspot. *Nature Geoscience* 5, 911–917.
- Koppers, A.A.P., Yamazaki, T., Geldmacher, J. and the Expedition 330 Scientists (2012b). *Proceedings of the Integrated Ocean Drilling Pprogram 330*: Tokyo (Integrated Ocean Drilling Program Management International, Inc.). doi:10.2204/iodp.proc.330.2012. <http://publications.iodp.org/proceedings/330/330toc.htm>

- Le Bas, M.J., Le Maitre, R.W., Streckeisen, A., and Zanettin, B., 1986. A chemical classification of volcanic rocks based on the total alkali – silica diagram. *Journal of Petrology* 27, 745–750.
- Lonsdale, P. (1988). Geography and history of the Louisville Hotspot Chain in the southwest Pacific. *Journal of Geophysical Research* 93, 3078.
- Luyendyk, B. P. (1995). Hypothesis for Cretaceous rifting of east Gondwana caused by subducted slab capture. *Geology* 23, 373–376.
- Lyons, S. N., Sandwell, D. T. and Smith, W. H. F. (2000). Three-dimensional estimation of elastic thickness under the Louisville Ridge. *Journal of Geophysical Research* 105, 13239.
- Macdonald, G.A. and Katsura, T., 1964. Chemical composition of Hawaiian lavas. *Journal of Petrology* 5, 82–133.
- Mahoney, J.J. and Spencer, K.J. (1991). Isotopic evidence for the origin of the Manihiki and Ontong Java oceanic plateaus, *Earth and Planetary Science Letters* 104, 196–210.
- Mahoney, J.J., Fitton, J.G., Wallace, P.J., et al. (2001). *Proceedings of the Ocean Drilling Program, Initial Reports* 192. College Station, TX (Ocean Drilling Program).
doi:10.2973/odp.proc.ir.192.2001
- McDade, P., Blundy, J.D. and Wood, B.J. (2003). Trace element partitioning on the Tinaquillo lherzolite solidus at 1.5 GPa. *Physics of the Earth and Planetary Interiors* 139, 129–147.
- McDonough, W.F. and Sun, S.-s. (1995). The composition of the Earth. *Chemical Geology* 120, 223–253.

- McKenzie D. and Bickle M.J. (1988). The volume and composition of melt generated by extension of the lithosphere. *Journal of Petrology* 29, 625–629.
- McKenzie, D and O’Nions, R.K. (1991). Partial melt distributions from inversion of Rare earth element concentrations. *Journal of Petrology* 32, 1021–1091.
- McKenzie, D., Jackson, J. and Priestley, K. (2005). Thermal structure of oceanic and continental lithosphere. *Earth and Planetary Science Letters* 233, 337–349.
- Montgomery, A.F. and Johnson, P.H. (1987). Paleomagnetic studies on Leg 91 basalts and sediments. In Menard, H., Natland, J., Jordan, T., Orcutt, J. and et al. (1983). *Initial reports of the Deep Sea Drilling Program* 91. Washington DC: US Government. Printing Office 475–482.
- Morgan, W.J. (1971). Convection plumes in the lower mantle. *Nature* 230, 42–43.
doi:10.1038/230042a0.
- Mortimer, N., Hoernle, K., Hauff, F., Palin, J. M., Dunlap, W. J., Werner, R. and Faure, K. (2006). New constraints on the age and evolution of the Wishbone Ridge, southwest Pacific Cretaceous microplates, and Zealandia–West Antarctica breakup. *Geology* 34, 185.
- Müller, R. D., Sdrolias, M., Gaina, C. and Roest, W.R. (2008). Age, spreading rates, and spreading asymmetry of the world’s ocean crust. *Geochemistry Geophysics Geosystems* 9, Q04006, doi:10.1029/2007GC001743.
- Nichols, A. R. L., Beier, C., Brandl, P.A., Buchs, D.M. and Krumm, S.H. (2014). Geochemistry of volcanic glasses from the Louisville Seamount Trail (IODP Expedition 330): Implications for eruption environments and mantle melting. *Geochemistry Geophysics Geosystems* 15, doi:10.1002/2013GC005086.

- Niu, Y., Wilson, M., Humphreys, E.R. and O'Hara, M.J. (2011). The origin of intra-plate ocean island basalts (OIB): the lid effect and its geodynamic implications. *Journal of Petrology* 52, 1443–1468.
- Norrish, K. and Hutton, J.T. (1969). An accurate X-ray spectrographic method for the analysis of a wide range of geological samples, *Geochimica et Cosmochimica Acta* 33, 431–453.
- O'Connor, J. M., Steinberger, B., Regelous, M., Koppers, A.A.P., Wijbrans, J.R., K. M. Haase, K.M., Stoffers, P., Jokat, W. and Garbe-Schönberg, D. (2013), Constraints on past plate and mantle motion from new ages for the Hawaiian-Emperor Seamount Chain, *Geochemistry Geophysics Geosystems* 14, 4564–4584, doi:10.1002/ggge.20267.
- Olson, P., Schubert, G., Anderson, C. and Goldman, P. (1988). Plume formation and lithosphere erosion: a comparison of laboratory and numerical experiments. *Journal of Geophysical Research* 93, 15,065–15,084.
- Prestvik, T., Goldberg, S. and Goles, G.G. (1999). Petrogenesis of the volcanic suite of Bouvetoya (Bouvet Island), South Atlantic. *Norsk Geologisk Tidsskrift* 79, 205–218.
- Putirka, K., Ryerson, F. J., Perfit, M. and Ridley W. I. (2011). Mineralogy and composition of the oceanic mantle. *Journal of Petrology* 52, 279–313, doi:10.1093/petrology/egq080.
- Regelous, M., Hofmann, A.W., Abouchami, W. and Galer, S.J.G. (2003). Geochemistry of lavas from the Emperor Seamounts, and the geochemical evolution of Hawaiian magmatism from 85 to 42 Ma. *Journal of Petrology* 44, 113–140.
- Rhodes, J.M. (2015). Major-element and isotopic variations in Mauna Loa magmas over 600 ka: implications for magma generation and source lithology as Mauna Loa transits the Hawaiian plume. In *Hawaiian Volcanoes: from Source to Surface*. (Eds. Carey, R., Cayol, V.,

Poland, M. and Weis, D.) *Geophysical Monograph* 208, American Geophysical Union, Washington, D. C., 59–78.

Rhodes, J. M. and Vollinger, M.J., (2004). Composition of basaltic lavas sampled by phase-2 of the Hawaii Scientific Drilling Project: Geochemical stratigraphy and magma types, *Geochemistry Geophysics Geosystems* 5, doi:10.1029/2002GC000434.

Rogers, N.W., Thomas, L.E., Macdonald, R., Hawkesworth, C.J. and Mokadem, F. (2006). ^{238}U – ^{230}Th disequilibrium in recent basalts and dynamic melting beneath the Kenya rift. *Chemical Geology* 234, 148–168.

Salters, V.J.M., Longhi, J.E., Bizimis, M. (2002). Near mantle solidus trace element partitioning at pressures up to 3.4 GPa. *Geochemistry Geophysics Geosystems* 3(6), doi:10.1029/2001GC000148.

Sarafian, E., Gaetani, G.A., Hauri, E.H. and Sarafian, A.R. (2017). Experimental constraints on the damp peridotite solidus and oceanic mantle potential temperature. *Science* 355, 942–945.

Skulski, T., Minarik, W. and Watson, E.B. (1994). High-pressure experimental trace-element partitioning between clinopyroxene and basaltic melts. *Chemical Geology* 117, 127–147.

Sobolev, A. V., Hofmann, A. W., Sobolev, S. V. and Nikogosian, I. K. (2005). An olivine-free mantle source of Hawaiian shield basalts. *Nature* 434, 590–597

Sun, S-s. and McDonough, W.F. (1989). Chemical and isotopic systematics of oceanic basalts: implications for mantle composition and processes. In Saunders, A.D. and Norry, M.J. (Eds), *Magmatism in the Ocean Basins*. Geological Society Special Publication 42, pp. 313–345.

- Sutherland, R. and Hollis, C. (2001). Cretaceous demise of the Moa plate and strike-slip motion at the Gondwana margin. *Geology* 29, 279–282.
- Tarduno, J.A., Duncan, R.A., Scholl, D.W. et al. (2003). The Emperor Seamounts: southward motion of the Hawaiian hotspot plume in Earth's mantle. *Science* 301, 1064–9.
- Tejada, M. L. G., Hanyu, T., Ishikawa, A., Senda, R., Suzuki, K., Fitton, G. and Williams, R. (2015). Re-Os isotope and platinum group elements of a FOCal ZONE mantle source, Louisville Seamounts Chain, Pacific ocean, *Geochemistry Geophysics Geosystems* 16, 486–504, doi:10.1002/2014GC005629.
- Tejada, M.L.G., Mahoney, J.J., Castillo, P.R., Ingle, S.P., Sheth, H.C. and Weis, D. (2004). Pin-pricking the elephant: evidence on the origin of the Ontong Java Plateau from Pb-Sr-Hf-Nd isotopic characteristics of ODP Leg 192 basalts. In Fitton, J.G., Mahoney, J.J., Wallace, P.J. and Saunders, A.D. (Eds.), *Origin and Evolution of the Ontong Java Plateau*. Geological Society Special Publication 229, 133–150.
- Tuff, J. and Gibson, S. (2007). Trace-element partitioning between garnet, clinopyroxene and Fe-rich picritic melts at 3 to 7 GPa. *Contributions to Mineralogy and Petrology* 153, 369–387.
- Turcotte, D.L. and Schubert, G. (1982). *Geodynamics: Applications of Continuum Physics to Geological Problems*. New York: Wiley, 450 pp.
- Vanderkluyzen, L., Mahoney, J.J., Koppers, A.A.P., Beier, C., Regelous, M., Gee, J.S. and Lonsdale, P.F. (2014). Louisville Seamount Chain: Petrogenetic processes and geochemical evolution of the mantle source. *Geochemistry Geophysics Geosystems* 15, 2380–2400, doi:10.1002/2014GC005288.

Walter, M.J. (1998). Melting of garnet peridotite and the origin of komatiite and depleted lithosphere. *Journal of Petrology* 39, 29–60.

Watson, S. and McKenzie, D. (1991). Melt generation by plumes: a study of Hawaiian volcanism. *Journal of Petrology* 32, 501–537.

Watts, A. B., Weissel, J. K., Duncan, R. A. and Larson, R. L. (1988). Origin of the Louisville Ridge and its relationship to the Eltanin Fracture Zone System. *Journal of Geophysical Research* 93, 3051.

Wessel, P. (2016). Regional–residual separation of bathymetry and revised estimates of Hawaii plume flux. *Geophysical Journal International* 204, 932–947.

Worthington, T. J., Hekinian, R., Stoffers, P., Kuhn, T. and Hauff, F. (2006). Osbourn Trough: Structure, geochemistry and implications of a mid-Cretaceous paleosspreading ridge in the South Pacific. *Earth and Planetary Science Letters* 245, 685–701.

FIGURE CAPTIONS

Figure 1. Map of the Pacific Ocean showing the location of the Hawaii-Emperor seamount trail (HEST), the Louisville seamount trail (LST) and the Ontong Java Plateau (OJP). The two boxes show the locations of Figure 2 (a) and (b).

Figure 2. (a) Map showing the location of the north-western part of the Louisville seamount trail. Circles show the location of individual seamounts, with those drilled during IODP Expedition 330 highlighted in colour. The same colour coding is used for data from these seamounts in Figures 4–5, 7 and 8. U1372–1377 are the drill sites; seamount ages from Koppers et al. (2012a). The locations of previous DSDP and IODP drill sites north of Osbourn Trough are also shown. Ocean floor isochrons are based on Müller et al. (2008) and on the Agegrid data for ocean lithosphere from EarthByte.org.

(b) Map showing the location of the Emperor seamounts from which the data (from Regelous et al., 2003; Huang et al., 2005) used in this study were obtained. Seamount ages are from O'Connor et al. (2013). Ocean floor isochrons are based on Müller et al. (2008) and on the Agegrid data for ocean lithosphere from EarthByte.org.

Figure 3. Stratigraphic columns (depth in metres below sea floor) for the three deepest holes drilled in the Louisville seamounts during IODP Expedition 330 (based on detailed logs given in Koppers et al., 2012b). Data points show the location of the samples used in this study and the downhole variation in Nb/Zr.

Figure 4. A plot of total alkalis against silica (after Le Bas et al. 1986), showing the range of composition of volcanic rock samples with <2 wt.% loss on ignition recovered from the Louisville seamounts during IODP Expedition 330, and by dredging and drilling on the Emperor seamounts (from Regelous et al., 2003; Huang et al., 2005). All analyses have been recalculated to sum to 100 wt.% with Fe as FeO. The line separating Hawaiian tholeiitic and alkaline basalts is from Macdonald and Katsura (1964). The field of analyses of Louisville glass samples (from Nicholls et al., 2015) covering the same drilled interval as the whole-rock samples is shown in grey. Note that many of the least altered whole-rock samples appear to have lost alkalis.

Figure 5. Incompatible trace element concentrations, normalised to primitive mantle values (McDonough and Sun, 1995), in basaltic rock samples recovered from the Louisville seamounts during IODP Expedition 330 and from the Emperor seamounts by dredging and DSDP/ODP drilling (data from Regelous et al., 2003; Huang et al., 2005). The grey field on all panels shows the range of composition of all the Louisville samples for comparison. Data for primitive (Kroenke-type) Ontong Java Plateau tholeiitic basalt are from Fitton and Godard (2004).

Figure 6. Sr- and Nd-isotope ratios in basalt samples from the Louisville seamounts collected by dredging (Vanderkluisen et al., 2014) compared with data from the Emperor seamounts (Regelous et al. 2003; Huang et al., 2005) and the Ontong Java Plateau (Tejada et al., 2004). The two sets of OJP data points show the effect of age-correction. Site 884 is located on the outer flank of Detroit seamount. Data fields for basalt from the Hawaiian Islands (RNA, rejuvenated and North Arch) and East Pacific Rise (EPR) are taken from Huang et al., 2013.

Figure 7. Chondrite-normalised Sm/Yb plotted against chondrite-normalised Ce/Sm for basalt samples from the Emperor (data from Regelous et al., 2003; Huang et al., 2005) and Louisville seamounts. Data (from Fitton and Godard, 2004) for basalt from the Ontong Java Plateau (OJP) are included for comparison. (a) Partial melting curves are based on a mantle source composition derived from the composition of primitive OJP tholeiitic (Kroenke-type) basalt and are labelled with melt % and proportion of spinel- and garnet lherzolite in the source. (b) The melting curves are for a mantle source composed of a 50:50 mixture of peridotite and pyroxenite/eclogite. Details of the melting calculations are given in the text, and the D values used are given in Table 4.

Figure 8. Nb plotted against Zr for basalt samples from the Emperor (data from Regelous et al., 2003; Huang et al., 2005) and Louisville seamounts. Data for basalt from the Ontong Java Plateau (OJP) are included for comparison. (a) Partial melting curves are based on a peridotite mantle source composition derived from the composition of primitive OJP tholeiitic (Kroenke-type) basalt and are labelled with melt % and proportion of spinel- and garnet lherzolite in the source. (b) The melting curves are for a mantle source composed of a 50:50 mixture of peridotite and pyroxenite/eclogite. Details of the melting calculations are given in the text, and the D values used are given

in Table 4. The late-stage samples from Burton seamount include two glass analyses from Nicholls et al. (2015).

Figure 9. A decompression melting model for mantle with potential temperature (T_p) of 1300, 1400 and 1500°C. The mantle has an adiabatic gradient of 0.3°C/km (Turcotte and Schubert, 1982) until it crosses the dry solidus and cools at a faster rate, producing melt at 0.4%/km (Klein and Langmuir, 1987). Decompression and melting stop at the base of the lithosphere. The dry mantle solidus and the solidus of mantle with 0.05% water are from Katz et al. (2003), and the depth of the transition from spinel- to garnet lherzolite is from Klemme and O'Neil (2000).

Figure 10. Curves showing the variation of Nb/Zr and Ce/Y with lithosphere thickness in accumulated partial melts from mantle with $T_p=1300, 1400$ and 1500°C , based on the melting model shown in Figure 9. The black curves are for a peridotite mantle source; red curves are for a 50:50 mixture of peridotite and pyroxenite/eclogite. Nb/Zr and Ce/Y are calculated by summing the composition of partial melts in 1-km (0.4%) increments in a column of mantle extending from the depth of the dry solidus to the base of the lithosphere. The small arrows mark the points at which the curves cross the garnet-spinel transition, and the numbers give the % melt at various points along the curves. Lithosphere thickness for the data points is calculated from the age of the lithosphere at the time of eruption and the relationship between age and the depth to the 1100 °C isotherm in the plate model of McKenzie et al. (2005). Data from Detroit Seamount (Huang et al., 2005) and for samples from the shield-forming stage of the other Emperor seamounts (Regelous et al., 2003) plot close to the curve for $T_p=1500^\circ\text{C}$, and data from the post-shield stage plot between the curves for $T_p=1400^\circ\text{C}$ and 1300°C . This is consistent with the derivation of shield-forming magmas from the hotter axis of

a mantle plume and the post-shield magmas from the cooler plume sheath as the seamount drifts away from the plume axis. The mean composition (error bars show the full range of the data) of shield-forming lavas of Mauna Kea, sampled by the Hawaii Scientific Drilling Project (Rhodes and Vollinger, 2004), plots close to the curve for $T_p=1500^\circ\text{C}$. Data from the Louisville seamounts, by contrast, show no significant relationship between Nb/Zr and Ce/Y and lithosphere thickness at the time of seamount formation. C, Canopus; R, Rigil; B, Burton; A, Achernar; H, Hadar.

Figure 11. Plots of Nb/Zr and Ce/Y versus lithosphere age at the time of emplacement for the Louisville and Emperor seamounts compared with data from ocean island basalt (OIB) and mid-ocean ridge basalt (MORB). OIB data from Fitton (2007), except for Bouvet data which are from Prestvik et al (1999). Hawaiian Islands: Loihi, Hawaii, Kahoolawe, Lanai, Maui, Oahu, Kauai. Atlantic Ocean: An Annobon, As Ascension, Az Azores, Bk Bioko, Bv Bouvet, Ca Canaries, CV Cape Verde, FN Fernando de Noronha, G Gough, P Principe, SH St Helena, ST São Tomé, Td Trindade, Tr Tristan da Cunha. Indian Ocean: Ch Christmas, GC Grande Comore, Hd Heard, Ma Marion, Mo Moheli, Mt Mauritius, Rd Rodriguez, Re Réunion. Pacific Ocean: At Aitutaki, JF Juan Fernandez, Ks Kosrae, Pp Pohnpei, Ra Rapa, Ru Rurutu, Sm Samoa, Ta Tahiti, Tk Truk, UP Ua Pou. Principe and Rurutu are identified more than once on the diagram because they have a long history of volcanism. Average normal and enriched MORB (N-MORB and E-MORB) compositions are from Sun and McDonough (1989). The melting curves for $T_p=1300$, 1400 and 1500°C are for a peridotite mantle source as in Figure 10 but with lithosphere thickness converted to age. The curves for a peridotite-pyroxenite/eclogite mix shown on Figure 10 have been omitted from this diagram for clarity. Melt percentages along the right-hand side of the diagram are calculated for

garnet lherzolite with the composition of the Ontong Java Plateau mantle source. Details of the melting calculations are given in the text.

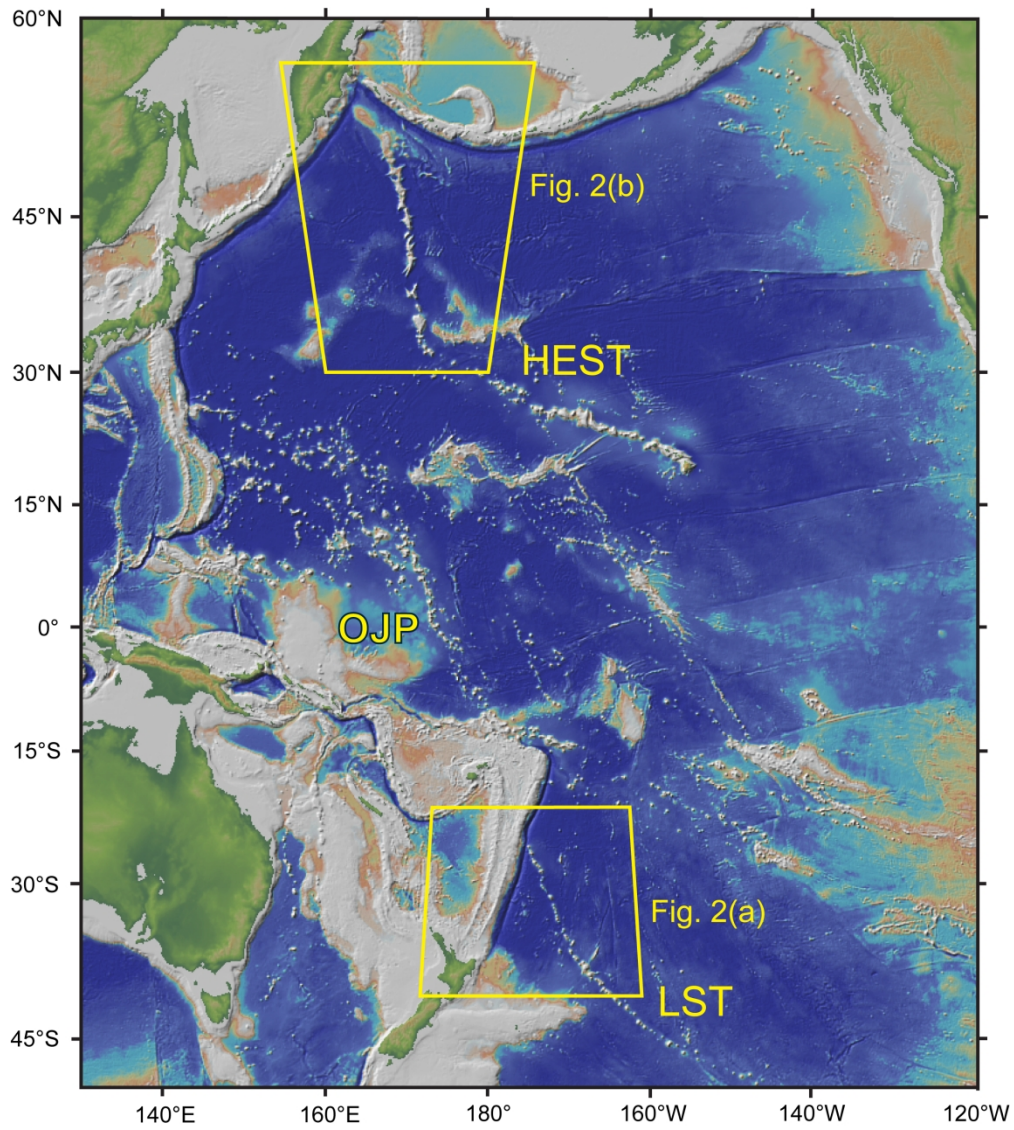


Figure 1. Map of the Pacific Ocean showing the location of the Hawaii-Emperor seamount trail (HEST), the Louisville seamount trail (LST) and the Ontong Java Plateau (OJP). The two boxes show the locations of Figure 2 (a) and (b).

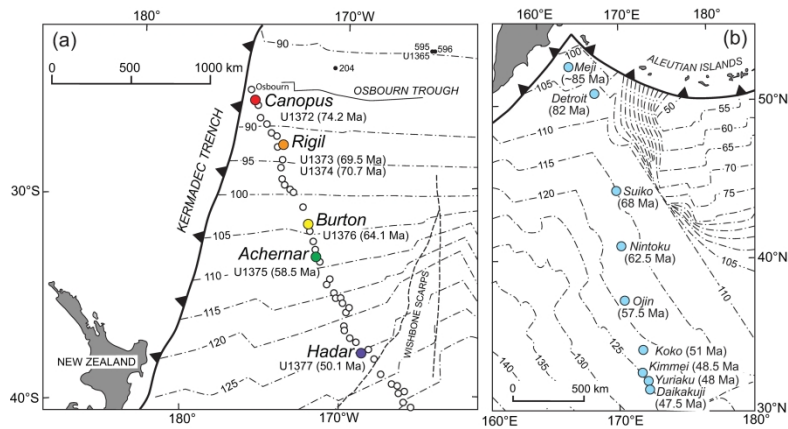


Figure 2. (a) Map showing the location of the north-western part of the Louisville seamount chain. Circles show the location of individual seamounts, with those drilled during IODP Expedition 330 highlighted in colour. The same colour coding is used for data from these seamounts in Figures 4–5, 7 and 8. U1372–1377 are the drill sites; seamount ages from Koppers et al. (2012a). The locations of previous DSDP and IODP drill sites north of Osborn Trough are also shown. Ocean floor isochrons are based on Müller et al. (2008) and on the Agegrid data for ocean lithosphere from EarthByte.org.

(b) Map showing the location of the Emperor seamounts from which the data (from Regélos et al., 2003; Huang et al., 2005) used in this study were obtained. Seamount ages are from O'Connor et al. (2013). Ocean floor isochrons are based on Müller et al. (2008) and on the Agegrid data for ocean lithosphere from EarthByte.org.

369x156mm (300 x 300 DPI)

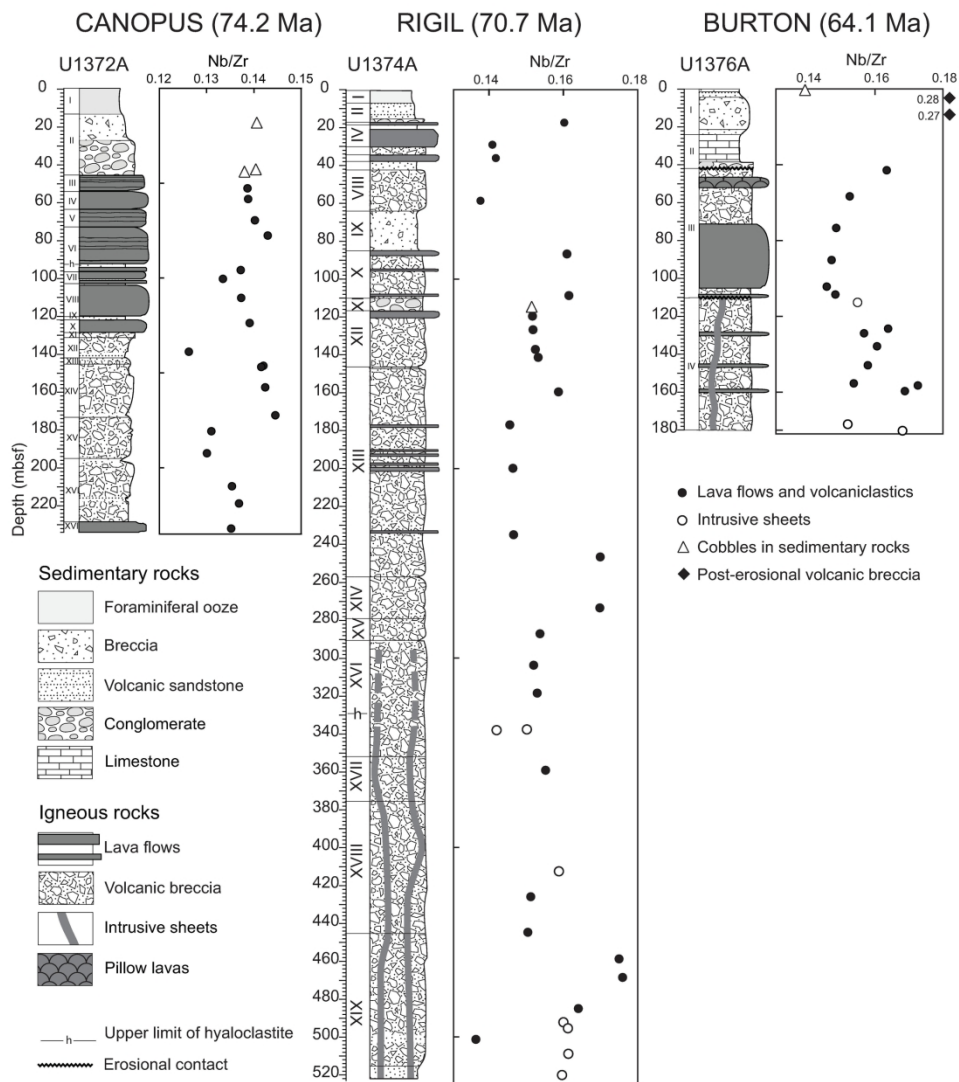


Figure 3. Stratigraphic columns (depth in metres below sea floor) for the three deepest holes drilled in the Louisville seamounts during IODP Expedition 330 (based on detailed logs given in Koppers et al., 2012b). Data points show the location of the samples used in this study and the downhole variation in Nb/Zr.

217x239mm (300 x 300 DPI)

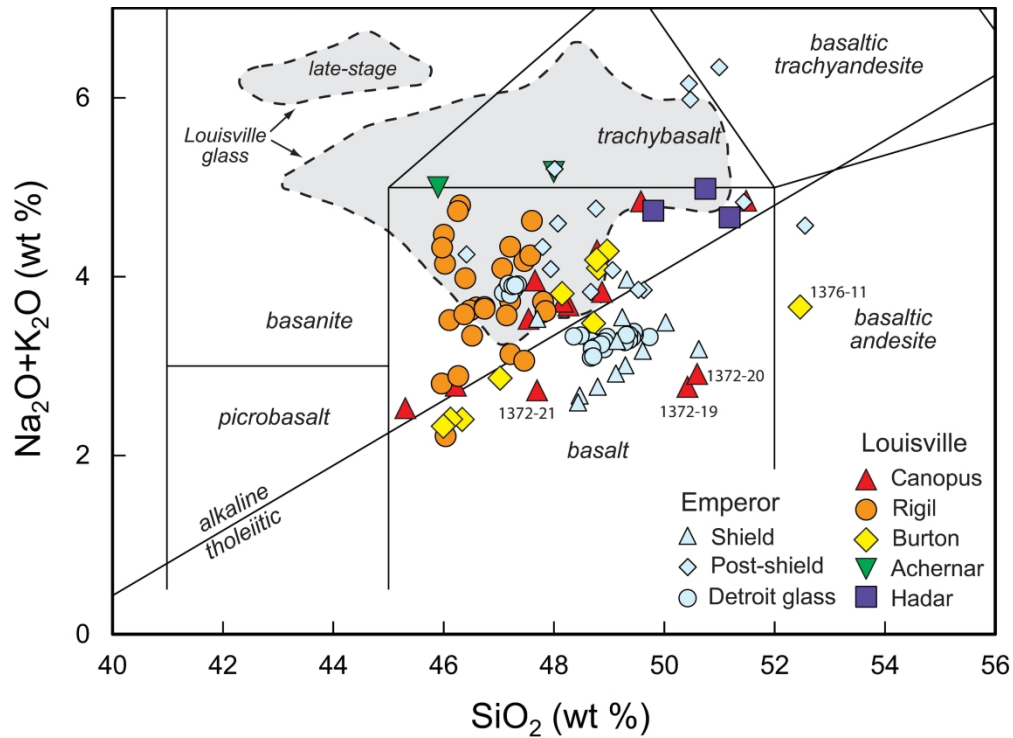
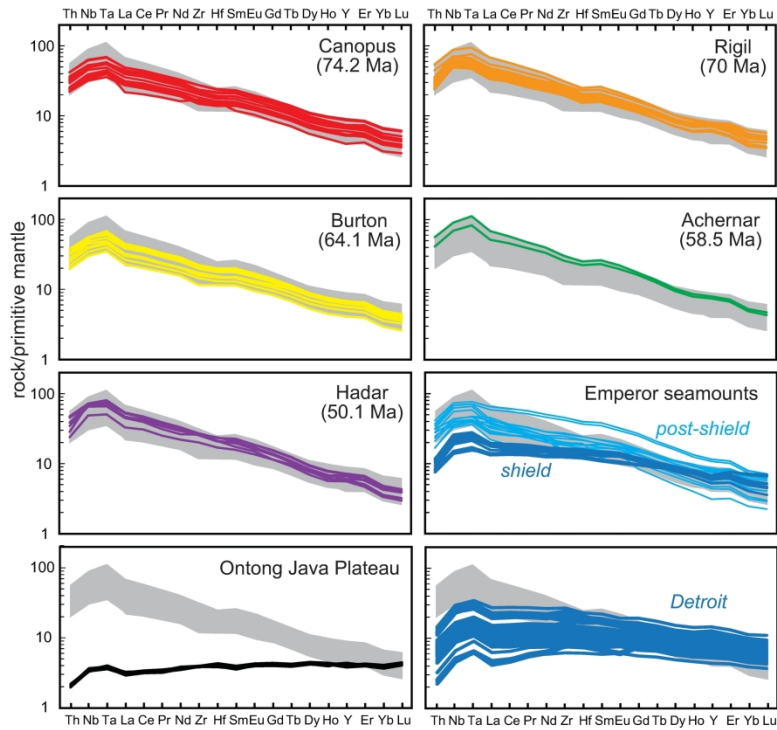


Figure 4. A plot of total alkalis against silica (after Le Bas et al. 1986), showing the range of composition of volcanic rock samples with <2 wt.% loss on ignition recovered from the Louisville seamounts during IODP Expedition 330, and by dredging and drilling on the Emperor seamounts (from Regelous et al., 2003; Huang et al., 2005). All analyses have been recalculated to sum to 100 wt.% with Fe as FeO. The line separating Hawaiian tholeiitic and alkaline basalts is from Macdonald and Katsura (1964). The field of analyses of Louisville glass samples (from Nicholls et al., 2015) covering the same drilled interval as the whole-rock samples is shown in grey. Note that many of the least altered whole-rock samples appear to have lost alkalis.

245x180mm (300 x 300 DPI)



Th Nb Ta La Ce Pr Nd Zr Hf Sm Eu Gd Tb Dy Ho Y Er Yb Lu

Figure 5. Incompatible trace element concentrations, normalised to primitive mantle values (McDonough and Sun, 1995), in basaltic rock samples recovered from the Louisville seamounts during IODP Expedition 330 and from the Emperor seamounts by dredging and DSDP/ODP drilling (data from Regelous et al., 2003; Huang et al., 2005). The grey field on all panels shows the range of composition of all the Louisville samples for comparison. Data for primitive (Kroenke-type) Ontong Java Plateau tholeiitic basalt are from Fitton and Godard (2004).

258x315mm (300 x 300 DPI)

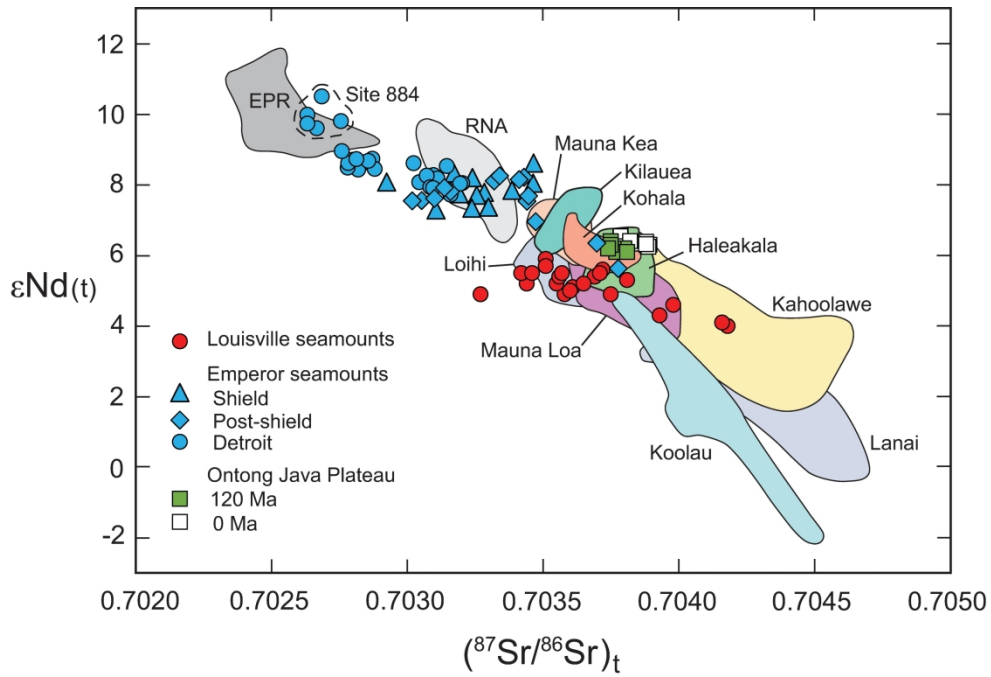


Figure 6. Sr- and Nd-isotope ratios in basalt samples from the Louisville seamounts collected by dredging (Vanderkluyssen et al., 2014) compared with data from the Emperor seamounts (Regelous et al. 2003; Huang et al., 2005) and the Ontong Java Plateau (Tejada et al., 2004). The two sets of OJP data points show the effect of age-correction. Site 884 is located on the outer flank of Detroit seamount. Data fields for basalt from the Hawaiian Islands (RNA, rejuvenated and North Arch) and East Pacific Rise (EPR) are taken from Huang et al., 2013.

244x165mm (300 x 300 DPI)

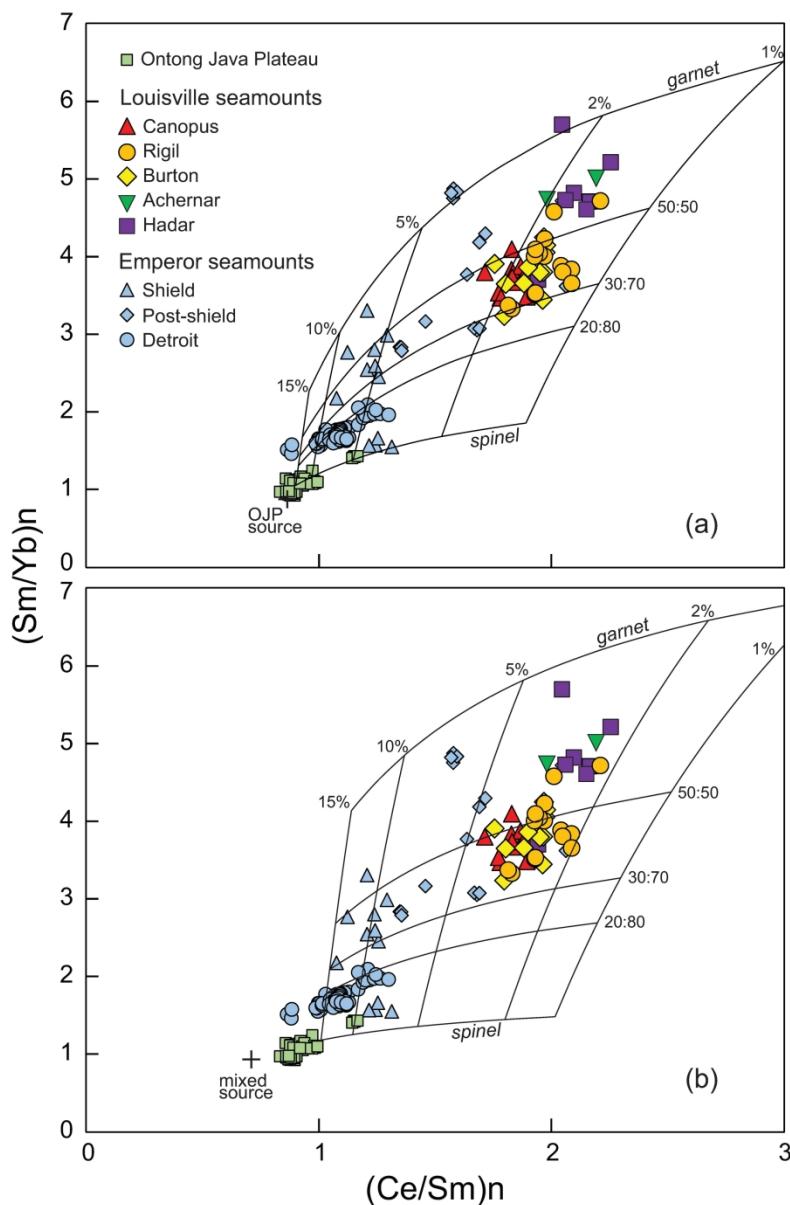


Figure 7. Chondrite-normalised Sm/Yb plotted against chondrite-normalised Ce/Sm for basalt samples from the Emperor (data from Regelous et al., 2003; Huang et al., 2005) and Louisville seamounts. Data (from Fitton and Godard, 2004) for basalt from the Ontong Java Plateau (OJP) are included for comparison. (a) Partial melting curves are based on a mantle source composition derived from the composition of primitive OJP tholeiitic (Kroenke-type) basalt and are labelled with melt % and proportion of spinel- and garnet lherzolite in the source. (b) The melting curves are for a mantle source composed of a 50:50 mixture of peridotite and pyroxenite/eclogite. Details of the melting calculations are given in the text, and the D values used are given in Table 4.

182x279mm (300 x 300 DPI)

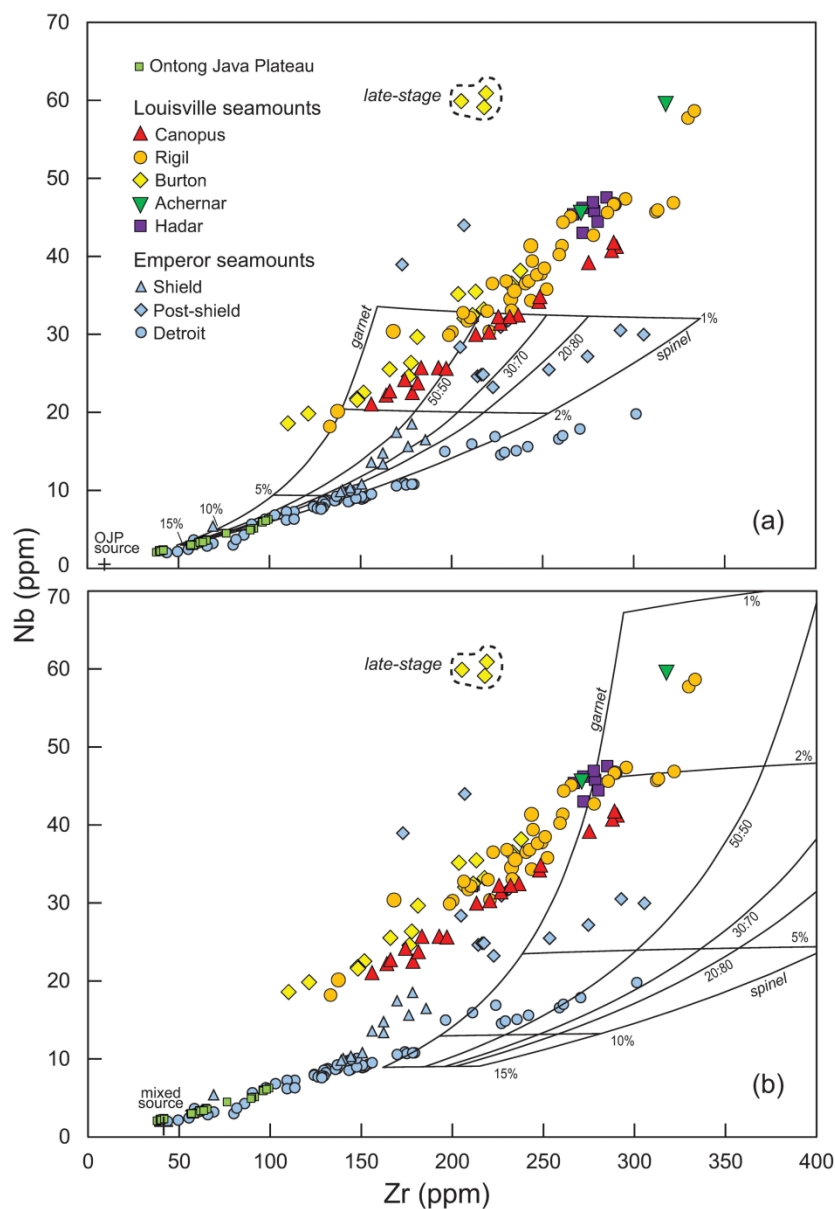


Figure 8. Nb plotted against Zr for basalt samples from the Emperor (data from Regelous et al., 2003; Huang et al., 2005) and Louisville seamounts. Data for basalt from the Ontong Java Plateau (OJP) are included for comparison. (a) Partial melting curves are based on a peridotite mantle source composition derived from the composition of primitive OJP tholeiitic (Kroenke-type) basalt and are labelled with melt % and proportion of spinel- and garnet lherzolite in the source. (b) The melting curves are for a mantle source composed of a 50:50 mixture of peridotite and pyroxenite/eclogite. Details of the melting calculations are given in the text, and the D values used are given in Table 4. The late-stage samples from Burton seamount include two glass analyses from Nicholls et al. (2015).

196x285mm (300 x 300 DPI)

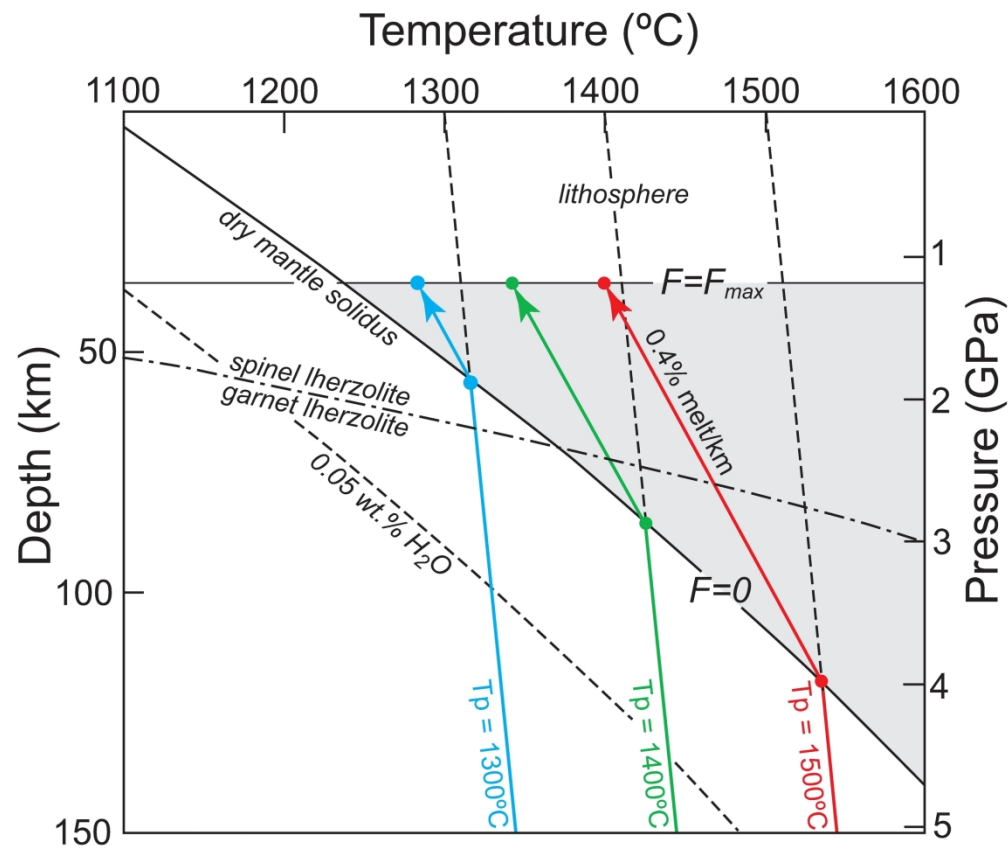


Figure 9. A decompression melting model for mantle with potential temperature (T_p) of 1300, 1400 and 1500°C. The mantle has an adiabatic gradient of 0.3°C/km (Turcotte and Schubert, 1982) until it crosses the dry solidus and cools at a faster rate, producing melt at 0.4%/km (Klein and Langmuir, 1987). Decompression and melting stop at the base of the lithosphere. The dry mantle solidus and the solidus of mantle with 0.05% water are from Katz et al. (2003), and the depth of the transition from spinel- to garnet lherzolite is from Klemme and O'Neil (2000).

237x201mm (300 x 300 DPI)

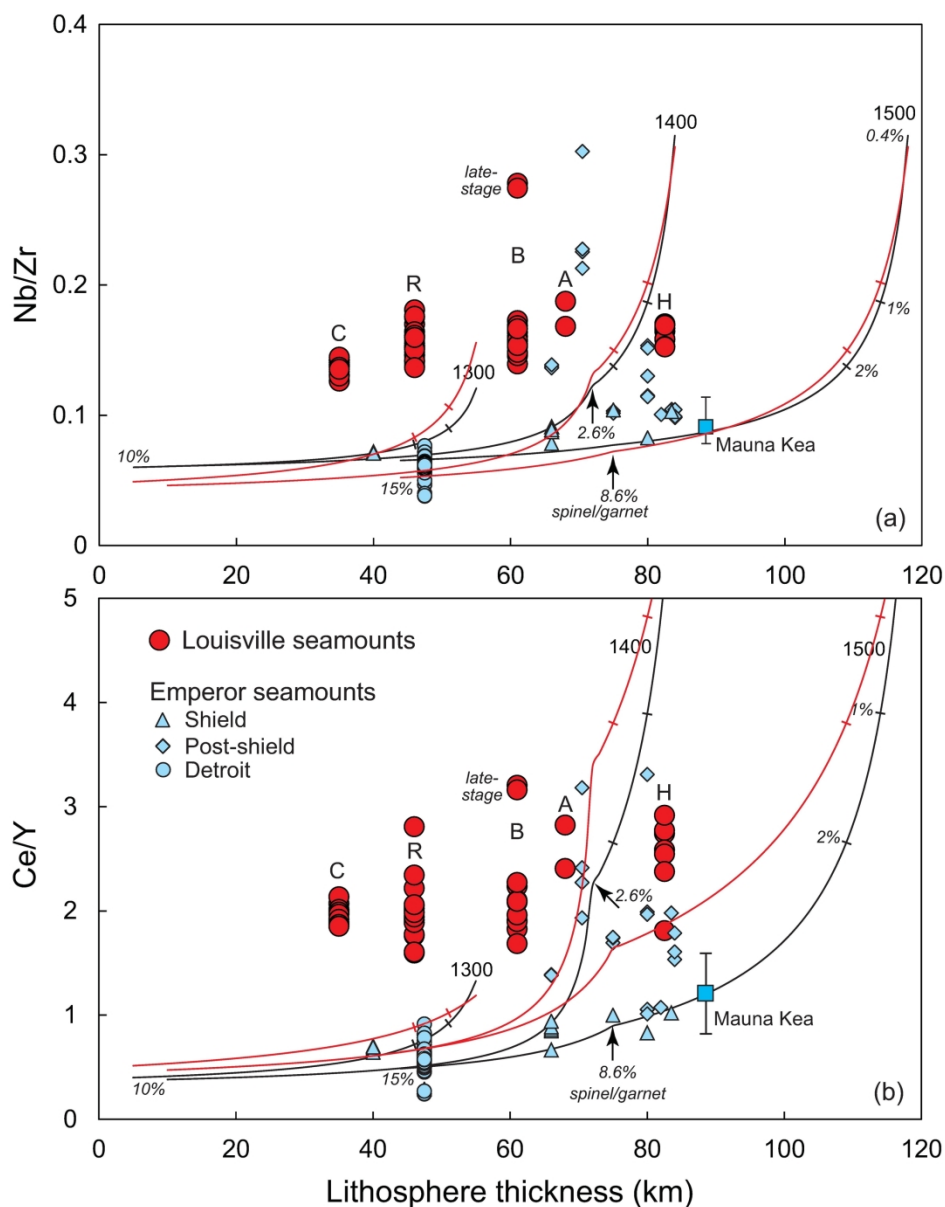


Figure 10. Curves showing the variation of Nb/Zr and Ce/Y with lithosphere thickness in accumulated partial melts from mantle with $T_p=1300$, 1400 and 1500°C , based on the melting model shown in Figure 9. The black curves are for a peridotite mantle source; red curves are for a 50:50 mixture of peridotite and pyroxenite/eclogite. Nb/Zr and Ce/Y are calculated by summing the composition of partial melts in 1-km (0.4%) increments in a column of mantle extending from the depth of the dry solidus to the base of the lithosphere. The small arrows mark the points at which the curves cross the garnet-spinel transition, and the numbers give the % melt at various points along the curves. Lithosphere thickness for the data points is calculated from the age of the lithosphere at the time of eruption and the relationship between age and the depth to the 1100°C isotherm in the plate model of McKenzie et al. (2005). Data from Detroit Seamount (Huang et al., 2005) and for samples from the shield-forming stage of the other Emperor seamounts (Regelous et al., 2003) plot close to the curve for $T_p=1500^\circ\text{C}$, and data from the post-shield stage plot between the curves for $T_p=1400^\circ\text{C}$ and 1300°C . This is consistent with the derivation of shield-forming magmas from the hotter axis of a mantle plume and the post-shield magmas from the cooler plume sheath as the seamount drifts away from the plume axis. The mean composition (error bars show the full range of

the data) of shield-forming lavas of Mauna Kea, sampled by the Hawaii Scientific Drilling Project (Rhodes and Vollinger, 2004), plots close to the curve for $T_p=1500^\circ\text{C}$. Data from the Louisville seamounts, by contrast, show no significant relationship between Nb/Zr and Ce/Y and lithosphere thickness at the time of seamount formation. C, Canopus; R, Rigil; B, Burton; A, Achernar; H, Hadar.

201x258mm (300 x 300 DPI)

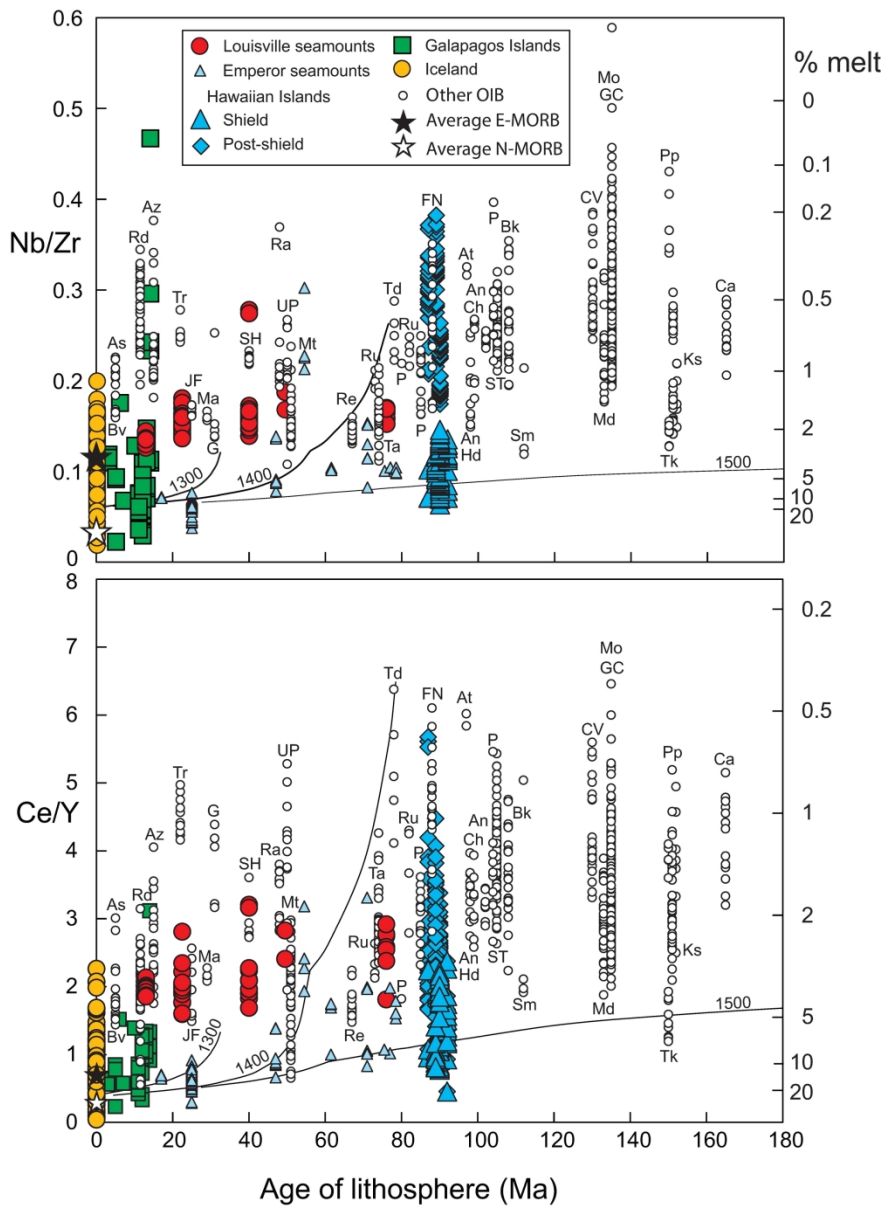


Figure 11. Plots of Nb/Zr and Ce/Y versus lithosphere age at the time of emplacement for the Louisville and Emperor seamounts compared with data from ocean island basalt (OIB) and mid-ocean ridge basalt (MORB). OIB data from Fitton (2007), except for Bouvet data which are from Prestvik et al (1999). Hawaiian Islands: Loihi, Hawaii, Kahooolawe, Lanai, Maui, Oahu, Kauai. Atlantic Ocean: An Annobon, As Ascension, Az Azores, Bk Bioko, Bv Bouvet, Ca Canaries, CV Cape Verde, FN Fernando de Noronha, G Gough, P Principe, SH St Helena, ST São Tomé, Td Trindade, Tr Tristan da Cunha. Indian Ocean: Ch Christmas, GC Grande Comore, Hd Heard, Ma Marion, Mo Moheli, Mt Mauritius, Rd Rodriguez, Re Réunion. Pacific Ocean: At Aitutaki, JF Juan Fernandez, Ks Kosrae, Pp Pohnpei, Ra Rapa, Ru Rurutu, Sm Samoa, Ta Tahiti, Tk Truk, UP Ua Pou. Principe and Rurutu are identified more than once on the diagram because they have a long history of volcanism. Average normal and enriched MORB (N-MORB and E-MORB) compositions are from Sun and McDonough (1989). The melting curves for $T_p=1300$, 1400 and 1500°C are for a peridotite mantle source as in Figure 910 but with lithosphere thickness converted to age. The curves for a peridotite-pyroxenite/eclogite mix shown on Figure 910 have been omitted from this diagram for clarity. Melt percentages along the right-hand side of the diagram are calculated for garnet lherzolite with the

composition of the Ontong Java Plateau mantle source. Details of the melting calculations are given in the text.

203x278mm (300 x 300 DPI)

Table 1. Major and trace element data for volcanic rocks from the Louisville seamounts recovered during IODP Expedition 330. Rock type abbreviations are L- lava, C – lava clast, sed – sedimentary conglomerate or breccia, B – volcanoclastic breccias, HB – hyaloclastite breccias, Int – intrusive sheet. Phenocryst mineralogies abbreviations are Ol – olivine, Pl – plagioclase, Cp – clinopyroxene, Aphyric (<1% phenocrysts), H – highly-phyric (>10% phenocrysts), M – moderately-phyric (>2%–10% phenocrysts), S – sparsely phyric (1%–2% phenocrysts).

Seamount	Canopus	Canopus	Canopus	Canopus	Canopus	Canopus	Canopus	Canopus
Sample #	1372-1	1372-2	1372-3	1372-4	1372-5	1372-6	1372-7	1372-8
Site, hole	U1372A	U1372A	U1372A	U1372A	U1372A	U1372A	U1372A	U1372A
Core-section	5R-1	8R-1	8R-2	9R-1	9R-6	10R-7	11R-6	13R-5
Interval (cm)	66-71	126-131	117-123	103-108	12-17	6-11	38-43	26-31
Depth (mbsf)	18.69	43.39	44.66	52.76	58.39	69.60	77.65	95.83
Rock type	C in sed	C in sed	C in sed	L	L	L	L	L
Phenocrysts	M-OI	M-OI	Aphyric	S-OI	H-OI	M-OI	Aphyric	Aphyric
XRF (wt %)								
SiO ₂	47.22	44.64	46.47	39.82	44.24	45.67	46.66	47.23
Al ₂ O ₃	15.34	12.75	15.24	15.16	11.33	15.43	15.09	14.54
Fe ₂ O ₃ T	11.85	12.79	12.55	15.01	13.61	12.85	12.78	12.21
MgO	6.12	13.68	5.80	4.03	16.29	3.94	6.57	5.02
CaO	11.66	8.50	10.98	12.28	8.27	10.96	11.40	11.24
Na ₂ O	2.77	2.07	2.93	2.59	1.82	2.74	2.68	3.07
K ₂ O	0.820	0.610	0.922	1.509	0.644	1.976	0.776	1.080
TiO ₂	2.690	2.325	3.266	3.069	2.325	3.040	2.877	3.018
MnO	0.144	0.168	0.162	0.172	0.176	0.127	0.169	0.205
P ₂ O ₅	0.395	0.328	0.444	0.462	0.299	0.492	0.419	0.423
LOI	1.09	1.96	1.08	5.83	0.96	2.46	0.69	1.78
Total	100.10	99.82	99.84	99.93	99.96	99.69	100.11	99.82
XRF (ppm)								
Zr	213.2	183.3	247.8	226.6	174.2	248.4	225.6	236.5
Nb	30.0	25.7	34.2	31.4	24.2	34.8	32.2	32.5
Y	28.4	23.7	31.0	28.8	22.7	31.7	30.0	30.5
Sr	483.8	361.9	557.8	540.1	387.3	513.7	485.5	467.7
Rb	14.4	10.3	15.4	16.7	11.0	24.5	11.4	18.7
Zn	98.1	89.4	100.6	121.5	94.6	112.5	93.9	105.4
Cu	66	42.2	78.3	63.2	63.6	72.1	86.1	70.1
Ni	74	376.9	60.7	293.8	512.9	82	72.9	107.3
Cr	130.8	779.2	111.1	504.3	803.9	110.9	94.5	137.7
V	287.3	230.8	289.7	341	211.2	410.3	317.1	313.5
Ba	154.7	122.9	180.4	174	120.4	195.6	176.2	161.6
Sc	32.3	23.9	28.2	34	22.6	35.7	30.2	30.8
ICP-MS (ppm)								
Y	28.30		32.50		23.60	34.05	30.63	
Zr	217.62		265.42		187.30	272.69	240.38	
Nb	28.26		34.56		24.29	36.20	32.69	
La	23.06		26.95		18.95	28.98	25.73	
Ce	53.77		64.24		45.45	67.72	60.45	
Pr	7.03		8.43		5.95	8.87	7.89	
Nd	30.46		36.44		25.73	38.01	33.64	
Sm	7.03		8.48		6.00	8.75	7.65	
Eu	2.27		2.71		1.91	2.82	2.51	
Gd	6.87		8.15		5.84	8.37	7.39	
Tb	1.03		1.21		0.87	1.23	1.11	
Dy	5.51		6.33		4.59	6.63	5.93	
Ho	1.06		1.19		0.87	1.25	1.13	
Er	2.71		2.97		2.19	3.21	2.92	
Yb	2.09		2.25		1.70	2.46	2.26	
Lu	0.29		0.31		0.24	0.34	0.31	
Hf	4.97		5.99		4.28	6.14	5.32	
Ta	1.81		2.16		1.54	2.13	2.04	
Th	2.33		2.72		1.93	2.90	2.47	

Seamount	Canopus	Canopus	Canopus	Canopus	Canopus	Canopus	Canopus	Canopus
Sample #	1372-9	1372-10	1372-11	1372-12	1372-13	1372-14	1372-15	1372-16
Site, hole	U1372A	U1372A	U1372A	U1372A	U1372A	U1372A	U1372A	U1372A
Core-section	14R-1	15R-1	16R-4	19R-1	21R-1	21R-2	23R-2	26R-2
Interval (cm)	71-78	118-123	30-35	64-69	124-130	44-50	5-11	44-50
Depth (mbsf)	100.45	110.51	123.73	138.87	146.27	146.92	157.66	172.36
Rock type	L	L	L	HB	C in B	C in B	C in B	C in B
Phenocrysts	M-OI, S-PI	Aphyric	Aphyric	Aphyric	S-PI	S-PI	M-PI	Aphyric
XRF (wt %)								
SiO ₂	45.27	47.15	47.49	48.94	47.83	47.29	46.19	50.35
Al ₂ O ₃	12.88	14.64	15.19	15.55	15.85	15.73	15.31	16.39
Fe ₂ O ₃ T	12.78	12.89	11.04	11.47	11.46	11.92	13.11	8.79
MgO	8.97	6.35	5.53	7.57	3.15	3.84	4.54	3.76
CaO	10.80	11.14	11.80	3.91	10.55	10.27	9.93	10.25
Na ₂ O	2.42	2.81	2.86	2.86	3.53	3.39	3.19	3.59
K ₂ O	0.739	0.827	0.855	0.829	1.139	0.934	0.985	1.150
TiO ₂	2.525	2.819	2.935	2.503	3.422	3.397	3.479	3.723
MnO	0.167	0.171	0.162	0.106	0.170	0.200	0.214	0.132
P ₂ O ₅	0.348	0.398	0.420	0.197	0.528	0.513	0.490	0.538
LOI	2.75	0.65	1.21	5.78	1.84	2.12	2.41	1.10
Total	99.65	99.85	99.49	99.72	99.46	99.59	99.84	99.77
XRF (ppm)								
Zr	192.8	220.5	231.8	178.4	290.4	287.7	275.1	288.9
Nb	25.7	30.3	32.2	22.5	41.2	40.7	39.2	41.8
Y	25.9	29.6	30.5	17.1	37.7	37.1	35.9	38.6
Sr	416.3	517.2	528.1	244.5	540.7	557.1	503.7	519.0
Rb	12.1	14.5	12.8	7.1	17.6	11.5	12.9	16.4
Zn	90	89.6	97.3	96.1	122.7	119.2	112.8	118.8
Cu	48.9	83.1	87.4	78.7	55.3	54.9	54.4	58.8
Ni	291.5	54.6	74.9	63.3	62.9	57.7	34.9	86.5
Cr	465.5	85.9	38.4	130.6	31.1	29.8	50.1	60.0
V	254.6	276.6	314.3	332.4	342	326.2	321.9	375
Ba	134.5	162.8	174.7	63.5	200.6	220	199.6	207.4
Sc	27.9	30.4	30.1	37	28	26.4	25.7	30.7
ICP-MS (ppm)								
Y	25.80		30.84	18.02		38.37		39.17
Zr	200.70		243.19	197.89		301.49		300.30
Nb	25.44		31.91	22.73		39.90		40.72
La	20.31		25.58	14.11		31.54		31.78
Ce	48.64		60.38	34.02		73.06		74.11
Pr	6.39		7.82	4.67		9.43		9.70
Nd	27.67		33.55	20.18		40.04		41.20
Sm	6.41		7.72	4.79		9.22		9.44
Eu	2.08		2.50	1.60		2.94		3.03
Gd	6.22		7.46	4.62		8.92		9.14
Tb	0.93		1.12	0.71		1.34		1.38
Dy	5.03		5.92	3.73		7.23		7.47
Ho	0.95		1.14	0.70		1.42		1.45
Er	2.45		2.91	1.83		3.61		3.72
Yb	1.87		2.22	1.37		2.86		2.95
Lu	0.26		0.31	0.20		0.40		0.41
Hf	4.54		5.46	4.52		6.69		6.82
Ta	1.65		2.02	1.64		2.51		2.57
Th	2.03		2.60	1.76		3.32		3.33

Seamount	Canopus	Canopus	Canopus	Canopus	Canopus	Rigil	Rigil	Rigil
Sample #	1372-17	1372-18	1372-19	1372-20	1372-21	1373-1	1373-2	1373-3
Site, hole	U1372A	U1372A	U1372A	U1372A	U1372A	U1373A	U1373A	U1373A
Core-section	28R-1	30R-2	33R-1	35R-1	38R-3	1R-2	2R-3	7R-2
Interval (cm)	53-58	105-110	76-81	20-25	86-92	142-148	46-51	68-75
Depth (mbsf)	180.76	192.37	209.79	218.83	232.10	2.25	12.76	34.66
Rock type	HB	HB	B	C in B	L	C in B	C in B	L
Phenocrysts	Aphyric	Aphyric	M-OI-PI	M-OI	M-OI-PI	H-OI	M-OI	H-OI-Cp
XRF (wt %)								
SiO ₂	49.86	51.74	48.87	49.02	46.26	45.29	43.53	43.02
Al ₂ O ₃	14.61	15.19	15.82	15.86	14.96	12.08	15.06	11.31
Fe ₂ O ₃ T	12.22	10.70	9.06	8.97	10.78	12.32	13.98	12.61
MgO	6.31	5.71	5.58	5.43	9.09	13.87	5.31	13.31
CaO	5.71	5.05	13.16	13.00	11.83	11.39	10.42	11.86
Na ₂ O	2.85	2.85	2.25	2.33	2.10	1.66	2.75	2.17
K ₂ O	0.911	0.996	0.426	0.482	0.540	0.513	1.629	0.716
TiO ₂	2.587	2.709	2.232	2.249	2.098	2.069	3.214	2.264
MnO	0.113	0.078	0.139	0.141	0.143	0.170	0.143	0.181
P ₂ O ₅	0.166	0.156	0.292	0.296	0.272	0.244	0.508	0.359
LOI	4.28	4.45	1.71	1.63	1.31	0.35	3.21	2.21
Total	99.62	99.63	99.54	99.42	99.38	99.96	99.75	100.01
XRF (ppm)								
Zr	181.4	197.0	164.1	166.1	155.9	137.5	243.4	168.0
Nb	23.8	25.6	22.2	22.7	21.1	20.1	41.3	30.4
Y	17.4	14.5	23.3	24.0	22.3	20.4	28.2	20.7
Sr	315.0	276.1	476.9	482.7	437.0	377.2	502.8	525.7
Rb	10.0	11.5	3.9	4.3	8.9	10.8	20.1	13.6
Zn	92.2	84	104.4	104	76	79.4	115	84.5
Cu	93.4	162	84.2	83.8	79.3	77	44.3	73
Ni	83.5	80.9	87.8	83.8	175.6	325.3	190.1	368.7
Cr	364.7	347.6	532.8	544.0	481.3	794.1	260.8	717.3
V	294.9	342	255	252.6	232.9	269.6	347	234.4
Ba	52.6	87.4	104.9	114	113.5	101.8	227.8	194.1
Sc	37.2	41.9	33.9	33.7	31.4	33.2	28	27.3
ICP-MS (ppm)								
Y			24.97		23.39			
Zr			178.49		168.60			
Nb			23.91		21.28			
La			18.39		17.69			
Ce			43.62		41.35			
Pr			5.74		5.52			
Nd			24.98		23.88			
Sm			5.92		5.63			
Eu			1.97		1.87			
Gd			5.81		5.56			
Tb			0.88		0.84			
Dy			4.80		4.53			
Ho			0.93		0.87			
Er			2.37		2.23			
Yb			1.85		1.73			
Lu			0.26		0.24			
Hf			4.09		3.90			
Ta			1.46		1.33			
Th			1.90		1.77			

Seamount	Rigil	Rigil	Rigil	Rigil	Rigil	Rigil	Rigil	Rigil
Sample #	1373-4	1373-5	1373-6	1374-1	1374-2	1374-3	1374-4	1374-5
Site, hole	U1373A	U1373A	U1373A	U1374A	U1374A	U1374A	U1374A	U1374A
Core-section	9R-1	11R-3	13R-2	3R-3	5R-4	7R-2	12R-1	16R-2
Interval (cm)	71-73	3-8	77-83	11-14	33-39	46-51	20-25	65-70
Depth (mbsf)	42.82	54.02	62.96	17.41	29.06	36.13	58.63	86.70
Rock type	L	L	L	L	L	L	B	L
Phenocrysts	Aphrylic	Aphrylic	Aphrylic	H-OI-Cp	Aphrylic	Aphrylic	M-OI	Aphrylic
XRF (wt %)								
SiO ₂	45.09	46.63	46.79	45.80	45.83	46.00	42.65	45.03
Al ₂ O ₃	15.11	14.83	15.02	14.71	15.47	15.44	16.04	17.00
Fe ₂ O ₃ T	13.03	12.73	12.70	11.70	14.86	14.36	13.87	13.57
MgO	4.94	5.89	5.80	9.11	5.82	5.57	4.10	5.33
CaO	11.56	11.49	11.57	9.01	8.96	8.95	11.68	9.25
Na ₂ O	2.84	2.86	2.83	2.78	3.12	3.16	2.60	3.08
K ₂ O	1.244	0.763	0.701	0.818	0.860	0.880	0.956	0.784
TiO ₂	2.975	3.012	3.034	2.614	3.288	3.346	2.687	3.647
MnO	0.215	0.172	0.163	0.181	0.210	0.191	0.173	0.183
P ₂ O ₅	0.450	0.445	0.447	0.618	0.443	0.457	0.553	0.558
LOI	2.37	0.68	0.87	2.04	1.03	1.34	4.11	1.07
Total	99.82	99.50	99.93	99.38	99.89	99.69	99.42	99.50
XRF (ppm)								
Zr	232.4	234.4	234.4	295.4	243.5	252.1	220.6	289.6
Nb	34.5	35.6	35.6	47.3	34.3	35.8	30.4	46.6
Y	32.1	32.1	31.8	32.0	34.9	35.6	31.6	35.0
Sr	442.7	467.8	484.7	586.1	441.9	444.7	490.7	703.0
Rb	18.3	9.1	6.3	8.9	14.5	13.3	15.7	8.6
Zn	107	96.7	95.8	104.4	105.8	112.2	117.2	97.3
Cu	66	100.5	100.4	41.6	37.2	36.9	54.6	36.8
Ni	58.4	60.6	60.5	191.7	31.4	30.1	156.2	36.2
Cr	65.3	51.5	50.8	442.1	25.3	26.6	400.4	12.6
V	347	332	330.5	204.5	340.7	356	348.7	282.2
Ba	185	187.1	184.7	230.5	173.9	180.3	156.1	230.6
Sc	34.5	32.9	31.6	17.4	26.7	28.5	35.8	20.5
ICP-MS (ppm)								
Y	31.29	31.03			33.68			33.47
Zr	234.25	229.79			235.57			279.70
Nb	36.22	35.58			34.34			46.23
La	24.80	24.55			24.29			31.08
Ce	56.68	56.95			55.71			70.87
Pr	7.29	7.27			7.33			9.07
Nd	31.41	31.35			31.77			38.46
Sm	7.09	7.12			7.35			8.35
Eu	2.32	2.27			2.36			2.65
Gd	6.92	6.93			7.11			7.65
Tb	1.03	1.04			1.09			1.15
Dy	5.65	5.64			5.96			6.06
Ho	1.08	1.08			1.15			1.17
Er	2.82	2.81			2.99			3.01
Yb	2.19	2.19			2.40			2.37
Lu	0.32	0.32			0.34			0.35
Hf	4.85	4.90			5.12			5.80
Ta	1.85	1.85			1.80			2.35
Th	2.19	2.24			2.22			2.67

Seamount	Rigil	Rigil	Rigil	Rigil	Rigil	Rigil	Rigil	Rigil
Sample #	1374-6	1374-7	1374-8	1374-9	1374-10	1374-11	1374-12	1374-13
Site, hole	U1374A	U1374A	U1374A	U1374A	U1374A	U1374A	U1374A	U1374A
Core-section	21R-2	22R-4	23R-3	25R-1	27R-2	28R-1	30R-5	32R-3
Interval (cm)	77-82	68-73	106-111	109-112	53-58	132-135	18-25	128-135
Depth (mbsf)	108.69	115.72	119.52	126.71	137.12	141.34	159.49	176.89
Rock type	L	C in B	L	C in B	C in B	C in B	L	L
Phenocrysts	Aphyric	H-OI-Cp	M-PI-OI-Cp	H-PI-OI-Cp	H-PI-OI-Cp	H-PI-OI-Cp	M-OI-PI	S-OI
XRF (wt %)								
SiO ₂	45.04	44.96	45.42	45.02	44.41	45.42	45.28	46.37
Al ₂ O ₃	16.79	14.58	14.93	15.00	15.02	15.09	14.68	15.93
Fe ₂ O ₃ T	14.29	13.15	13.00	13.02	12.75	13.09	12.53	13.04
MgO	5.39	8.97	8.92	7.60	6.93	7.56	8.74	6.51
CaO	9.37	9.19	10.07	10.62	11.15	10.32	10.07	8.61
Na ₂ O	3.08	2.60	2.59	2.66	2.64	2.68	2.73	3.42
K ₂ O	0.969	0.925	0.666	0.840	0.774	0.875	0.791	1.080
TiO ₂	3.623	2.798	2.739	2.758	2.751	2.812	2.644	2.972
MnO	0.183	0.179	0.179	0.192	0.205	0.190	0.204	0.197
P ₂ O ₅	0.555	0.450	0.427	0.441	0.449	0.456	0.455	0.588
LOI	0.23	1.93	1.06	1.61	2.38	1.37	1.69	0.98
Total	99.52	99.73	100.00	99.77	99.45	99.86	99.81	99.70
XRF (ppm)								
Zr	289.3	249.0	240.5	242.3	246.7	250.9	260.5	321.6
Nb	46.7	37.7	36.5	36.8	37.6	38.4	41.3	46.8
Y	34.6	30.6	29.9	30.0	30.0	30.8	31.3	34.8
Sr	692.5	467.6	520.0	534.3	539.0	541.9	522.0	603.9
Rb	15.8	16.0	10.9	14.9	13.5	16.2	12.8	15.4
Zn	98.7	87.2	92.7	98.9	99.3	99.5	95.9	92.7
Cu	35	46.9	50.8	50.3	48.9	49.3	46.4	35.4
Ni	34.4	173.6	154.1	165.4	156.6	154	155.9	78.8
Cr	13.9	265.1	279.2	289.7	253.6	262.7	316.1	101.0
V	278.8	247.7	252.1	260.2	260.7	263	237	226.5
Ba	214.8	170.4	175.3	157.8	156.8	168.7	184.1	227.5
Sc	22.4	22.7	25.4	26.3	25.3	25.8	23.3	20.8
ICP-MS (ppm)								
Y	33.74						30.67	
Zr	283.61						251.09	
Nb	47.10						40.76	
La	31.28						27.42	
Ce	70.91						62.28	
Pr	9.08						7.84	
Nd	38.44						32.94	
Sm	8.39						7.20	
Eu	2.63						2.28	
Gd	7.71						6.77	
Tb	1.13						1.01	
Dy	6.02						5.43	
Ho	1.15						1.05	
Er	3.00						2.73	
Yb	2.35						2.14	
Lu	0.34						0.31	
Hf	5.73						5.15	
Ta	2.34						2.07	
Th	2.60						2.57	

Seamount	Rigil	Rigil	Rigil	Rigil	Rigil	Rigil	Rigil	Rigil
Sample #	1374-14	1374-15	1374-16	1374-17	1374-18	1374-19	1374-20	1374-21
Site, hole	U1374A	U1374A	U1374A	U1374A	U1374A	U1374A	U1374A	U1374A
Core-section	37R-3	41R-4	42R-5	45R-4	46R-7	48R-5	50R-2	52R-2
Interval (cm)	39-44	55-58	105-111	58-63	73-76	97-102	31-36	39-45
Depth (mbsf)	199.86	234.92	246.63	273.54	287.18	303.79	318.54	337.69
Rock type	L	L	L	C in B	C in B	C in B	L	Int
Phenocrysts	S-OI	S-OI	M-Pl-Cp	S-Pl	M-Pl-Cp	M-Pl-Cp-OI	M-Pl-Cp-OI	Aphyric
XRF (wt %)								
SiO ₂	45.71	46.42	44.89	45.20	46.02	45.75	46.34	45.70
Al ₂ O ₃	15.88	15.92	15.72	15.88	14.89	15.69	15.82	14.98
Fe ₂ O ₃ T	13.13	13.09	12.68	12.18	13.63	12.09	12.01	13.00
MgO	6.54	7.14	5.85	5.67	5.29	5.55	5.97	5.96
CaO	8.93	8.42	12.08	12.28	11.09	12.70	12.36	8.91
Na ₂ O	3.27	3.24	2.60	2.62	2.87	2.32	2.40	3.17
K ₂ O	0.922	0.895	0.816	0.863	0.755	0.712	0.582	1.022
TiO ₂	3.006	3.046	3.290	3.275	3.502	2.727	2.779	3.271
MnO	0.180	0.164	0.180	0.192	0.272	0.185	0.189	0.275
P ₂ O ₅	0.573	0.570	0.525	0.526	0.531	0.393	0.389	0.408
LOI	1.37	1.21	1.13	1.24	0.77	1.57	0.83	2.73
Total	99.51	100.10	99.76	99.93	99.62	99.69	99.67	99.42
XRF (ppm)								
Zr	312.0	313.0	265.2	261.1	277.7	208.7	210.1	219.5
Nb	45.7	45.9	45.1	44.3	42.7	31.7	32.1	33.0
Y	34.5	34.7	31.1	30.9	34.6	26.7	27.1	29.8
Sr	609.0	596.9	643.4	637.3	562.9	507.1	514.6	453.8
Rb	11.6	11.3	12.8	14.2	10.7	18.0	12.2	12.7
Zn	95.3	95.9	97.5	98.1	118.9	98	95.3	122.4
Cu	34.1	33.8	81	82.1	50.2	64.1	64.4	104.4
Ni	94	106.7	57.9	62.7	34.8	71.2	73.6	51.9
Cr	120.2	125.5	87.2	98.1	12.6	180.0	175.7	40.2
V	236.4	226.3	296.9	304	359.8	295.4	289.9	425.4
Ba	216.7	214.1	214.1	211.5	218	121	139.6	168.5
Sc	21.9	20.5	27	27	29.2	32.3	31.7	35.3
ICP-MS (ppm)								
Y					32.57		26.88	
Zr					264.38		202.96	
Nb					41.87		32.20	
La					28.70		22.29	
Ce					66.23		51.19	
Pr					8.50		6.56	
Nd					36.56		28.36	
Sm					8.12		6.41	
Eu					2.55		2.07	
Gd					7.62		6.11	
Tb					1.13		0.90	
Dy					6.06		4.85	
Ho					1.14		0.91	
Er					2.92		2.32	
Yb					2.20		1.74	
Lu					0.31		0.25	
Hf					5.65		4.39	
Ta					2.15		1.79	
Th					2.34		2.01	

Seamount	Rigil							
Sample #	1374-22	1374-23	1374-24	1374-25	1374-26	1374-27	1374-28	1374-29
Site, hole	U1374A							
Core-section	52R-2	54R-4	60R-1	61R-3	63R-3	64R-6	65R-7	67R-5
Interval (cm)	78-83	30-36	16-21	118-123	112-117	101-104	104-110	70-75
Depth (mbsf)	338.08	359.21	412.59	426.00	444.77	458.80	468.60	485.04
Rock type	Int	C in HB	Int	C in B	L	C in B	C in B	C in B
Phenocrysts	Aphyric	Aphyric	Aphyric	M-PI	M-PI	Aphyric	Aphyric	Aphyric
XRF (wt %)								
SiO ₂	45.85	45.65	44.79	45.00	44.35	45.17	45.18	45.43
Al ₂ O ₃	14.67	14.76	15.31	16.78	16.37	17.19	17.30	15.15
Fe ₂ O ₃ T	12.85	13.99	12.29	12.87	12.48	12.82	12.67	12.24
MgO	5.87	4.83	6.09	5.66	5.83	4.86	4.77	7.17
CaO	10.11	11.53	11.33	12.72	12.46	9.52	9.77	13.14
Na ₂ O	3.07	2.64	2.65	2.37	2.36	3.81	3.76	2.37
K ₂ O	0.967	0.812	0.894	0.370	0.317	0.865	0.858	0.461
TiO ₂	3.092	3.323	2.691	2.887	2.787	3.682	3.709	2.864
MnO	0.262	0.206	0.147	0.162	0.160	0.187	0.190	0.162
P ₂ O ₅	0.433	0.491	0.390	0.362	0.355	0.734	0.731	0.429
LOI	2.33	1.27	3.01	0.38	2.50	0.89	1.08	0.48
Total	99.50	99.50	99.59	99.56	99.97	99.73	100.02	99.90
XRF (ppm)								
Zr	232.8	259.0	206.3	200.2	198.5	329.6	333.1	222.4
Nb	33.1	40.2	32.8	30.3	29.9	57.7	58.6	36.5
Y	33.8	32.5	25.9	26.7	26.9	34.5	34.4	25.7
Sr	386.7	526.1	646.1	558.6	556.2	924.8	932.7	566.3
Rb	12.8	24.2	12.9	5.6	3.4	16.2	15.9	9.5
Zn	111.7	122.4	96.5	98.5	95.7	98.1	100.3	96.3
Cu	48.4	57.3	60.1	90.7	91.0	32.4	32.9	115.2
Ni	39.9	46.1	48.5	58.2	58.0	12	12.3	94.5
Cr	26.5	29.1	34.7	57.4	58.6	6.5	4.7	86.3
V	363.2	357	286.6	332	330.4	230.1	226.2	295
Ba	172.4	157.5	245.9	143	153.1	293.8	301.8	172
Sc	24.7	29.7	23.9	28.5	28.0	15.8	16.4	31.4
ICP-MS (ppm)								
Y	33.13	32.82	25.61			35.86		25.50
Zr	229.71	253.22	205.14			345.42		215.61
Nb	33.51	40.60	33.00			59.98		36.21
La	23.08	27.18	21.61			44.32		24.41
Ce	54.31	63.16	51.52			96.92		57.05
Pr	7.08	8.10	6.59			12.24		7.16
Nd	31.09	34.80	28.38			50.34		30.72
Sm	7.23	7.83	6.44			10.58		6.85
Eu	2.28	2.49	2.09			3.31		2.19
Gd	7.01	7.34	6.09			9.42		6.29
Tb	1.08	1.10	0.91			1.33		0.92
Dy	5.88	5.84	4.76			6.86		4.78
Ho	1.14	1.10	0.89			1.27		0.88
Er	2.98	2.81	2.26			3.25		2.23
Yb	2.33	2.10	1.71			2.44		1.63
Lu	0.34	0.30	0.25			0.34		0.23
Hf	4.88	5.29	4.36			7.08		4.59
Ta	1.75	2.08	1.74			3.48		1.89
Th	1.94	2.47	1.89			4.27		2.10

Seamount	Rigil	Rigil	Rigil	Rigil	Rigil	Achernar	Achernar	Burton
Sample #	1374-30	1374-31	1374-32	1374-33	1374-34	1375-01	1375-02	1376-01
Site, hole	U1374A	U1374A	U1374A	U1374A	U1374A	U1375A	U1375B	U1376A
Core-section	68R-3	68R-5	69R-2	70R-1	72R-2	2R-1	1R-1	1R-1
Interval (cm)	23-28	82-89	127-137	60-65	86-92	30-33	10-15	140-145
Depth (mbsf)	492.22	495.44	501.30	508.93	520.10	8.82	0.13	1.43
Rock type	Int	Int	B	Int	Int	C in sed	L?	C in sed
Phenocrysts	Aphyric	Aphyric	Aphyric	Aphyric	Aphyric	Aphyric	M-OI	Aphyric
XRF (wt %)								
SiO ₂	44.98	42.65	42.37	45.15	44.86	46.30	44.22	41.44
Al ₂ O ₃	13.98	13.12	13.62	16.72	16.88	16.76	15.69	13.60
Fe ₂ O ₃ T	13.11	13.56	11.41	14.18	14.03	12.08	13.97	12.00
MgO	6.07	6.29	8.77	5.86	5.90	4.05	3.76	9.80
CaO	9.32	10.06	8.37	8.94	8.79	8.84	10.44	8.50
Na ₂ O	3.71	3.63	3.05	3.38	3.25	3.26	3.36	2.29
K ₂ O	1.157	1.162	0.921	1.000	0.967	1.722	1.456	1.462
TiO ₂	2.961	3.133	2.126	3.590	3.560	3.754	4.126	2.564
MnO	0.191	0.222	0.171	0.187	0.193	0.136	0.163	0.175
P ₂ O ₅	0.436	0.487	0.338	0.557	0.546	0.768	0.548	0.361
LOI	3.67	5.33	9.04	0.41	0.71	1.93	1.82	7.76
Total	99.59	99.64	100.19	99.97	99.68	99.60	99.56	99.95
XRF (ppm)								
Zr	229.9	244.2	133.2	288.9	285.5	317.6	271.0	176.5
Nb	36.8	39.4	18.2	46.6	45.6	59.5	45.6	24.6
Y	28.3	30.3	21.3	34.6	34.4	34.3	32.0	24.2
Sr	682.3	586.2	206.9	693.6	686.4	946.4	753.8	265.9
Rb	16.1	13.7	14.5	19.0	17.9	37.3	26.1	64.3
Zn	102.8	118.4	100	92.3	91.9	94.9	90	127.5
Cu	51.8	55.1	78	36	35.5	22.1	71	86.2
Ni	42.3	44.5	68.6	33.7	32.2	43.7	59.6	319.7
Cr	22.0	18.1	103.8	16.0	12.0	6.7	40.6	219.7
V	303	340.7	334.1	267	263.9	202.8	328.5	296.3
Ba	236.1	172.3	142.9	225.7	225.7	372.1	291.1	139.9
Sc	24.7	28.2	37.9	18.4	18.3	13.4	16.8	32.1
ICP-MS (ppm)								
Y		29.97		33.41	36.51	34.37	32.43	
Zr		236.33		271.90	310.67	343.28	290.01	
Nb		38.93		45.19	49.88	68.69	51.03	
La		25.74		30.75	35.20	44.42	33.45	
Ce		60.15		71.27	80.66	96.93	77.04	
Pr		7.66		8.90	10.30	12.06	9.96	
Nd		32.83		37.86	43.33	49.99	42.03	
Sm		7.37		8.25	9.51	10.67	9.39	
Eu		2.33		2.64	3.02	3.42	3.03	
Gd		6.92		7.50	8.78	9.50	8.82	
Tb		1.03		1.12	1.30	1.36	1.26	
Dy		5.44		5.93	6.89	6.96	6.45	
Ho		1.03		1.14	1.33	1.28	1.18	
Er		2.59		2.96	3.40	3.15	2.94	
Yb		1.90		2.34	2.72	2.32	2.16	
Lu		0.28		0.34	0.39	0.32	0.29	
Hf		5.05		5.76	6.55	7.14	6.32	
Ta		2.04		2.46	2.81	4.14	3.07	
Th		2.42		2.84	3.57	4.46	3.28	

Seamount	Burton	Burton	Burton	Burton	Burton	Burton	Burton	Burton
Sample #	1376-02	1376-03	1376-04	1376-05	1376-06	1376-07	1376-08	1376-09
Site, hole	U1376A	U1376A	U1376A	U1376A	U1376A	U1376A	U1376A	U1376A
Core-section	1R-4	2R-3	5R-4	6R-7	8R-5	11R-4	13R-3	14R-3
Interval (cm)	50-53	123-127	74-79	98-102	111-116	66-72	60-65	3-8
Depth (mbsf)	4.72	13.48	42.83	56.73	73.35	90.43	104.27	108.50
Rock type	C in sed	sed	HB	C in HB	L	L	L	L
Phenocrysts	H-OI	H-OI	H-OI-Cp	Aphyric	H-OI-Cp	H-OI-Cp	H-OI-Cp	H-OI-Cp
XRF (wt %)								
SiO ₂	39.74	24.44	42.62	47.46	45.17	45.00	44.99	45.69
Al ₂ O ₃	10.72	6.93	9.66	14.68	10.18	9.88	9.76	11.69
Fe ₂ O ₃ T	13.67	9.10	13.61	12.52	13.61	13.59	13.80	13.16
MgO	13.04	7.52	16.34	5.46	16.87	17.01	17.90	13.15
CaO	11.31	25.23	3.35	10.33	8.13	8.60	7.98	9.16
Na ₂ O	2.23	1.49	1.88	2.78	1.73	1.75	1.69	2.08
K ₂ O	1.250	1.098	1.027	1.368	0.608	0.590	0.580	0.699
TiO ₂	2.363	1.538	1.978	2.991	2.082	2.042	2.036	2.373
MnO	0.165	0.082	0.163	0.171	0.178	0.179	0.181	0.171
P ₂ O ₅	0.900	0.540	0.194	0.414	0.280	0.271	0.273	0.322
LOI	4.06	22.06	8.95	1.55	1.25	1.01	0.76	0.93
Total	99.45	100.03	99.77	99.72	100.09	99.93	99.95	99.42
XRF (ppm)								
Zr	218.9	118.3	121.4	217.6	151.7	148.1	148.2	177.7
Nb	60.9	32.5	19.8	33.2	22.5	21.8	21.6	26.3
Y	26.7	14.5	17.7	28.9	21.4	20.5	20.6	24.1
Sr	620.8	377.5	43.9	479.0	296.1	318.1	292.5	365.4
Rb	21.3	15.9	16.9	33.7	11.9	11.6	11.8	13.6
Zn	125.3	111.8	135.4	128.2	108.7	105.1	105.4	107.9
Cu	60.1	58.2	78.1	41.8	69.2	67.6	66.4	77.8
Ni	396.6	330.7	602.9	133.6	498.7	525.6	549.1	349.5
Cr	489.1	361.3	781.2	114.9	808.1	868.3	824.3	609.6
V	199.8	98	181.5	295.1	207.8	195.6	192.4	225.9
Ba	425.8	144.1	37.1	186.3	124.6	123.3	116.1	139.4
Sc	22.2	26.2	26.3	28.9	22.7	20.8	21.7	23.3
ICP-MS (ppm)								
Y			18.71	31.11	21.62			24.32
Zr			134.30	241.19	159.09			182.60
Nb			20.45	34.46	22.11			25.36
Ba			25.92	187.92	114.09			133.20
La			14.75	26.61	17.17			19.53
Ce			33.78	60.26	39.12			45.75
Pr			4.54	7.89	5.19			5.90
Nd			19.65	33.58	22.23			25.06
Sm			4.64	7.66	5.24			5.87
Eu			1.47	2.52	1.70			1.91
Gd			4.53	7.51	5.19			5.83
Tb			0.67	1.11	0.78			0.88
Dy			3.57	5.94	4.21			4.74
Ho			0.67	1.13	0.81			0.90
Er			1.72	2.86	2.05			2.29
Yb			1.29	2.16	1.56			1.75
Lu			0.17	0.30	0.22			0.24
Hf			3.25	5.37	3.70			4.16
Ta			1.30	-	1.48			1.69
Th			1.56	2.62	1.74			1.99

Seamount	Burton							
Sample #	1376-10	1376-11	1376-12	1376-13	1376-14	1376-15	1376-16	1376-17
Site, hole	U1376A							
Core-section	15R-2	17R-1	17R-3	18R-1	19R-1	21R-2	21R-2	21R-5
Interval (cm)	60-63	135-140	75-80	95-100	130-136	2-7	102-107	17-22
Depth (mbsf)	112.62	126.58	128.88	135.78	145.73	155.38	156.38	159.44
Rock type	Int	HB	L	L	L	C in B	L	L
Phenocrysts	Aphyric	Aphyric	Aphyric	Aphyric	S-OI	Aphyric	Aphyric	H-OI
XRF (wt %)								
SiO ₂	48.75	51.39	47.23	47.37	46.37	47.10	45.13	41.56
Al ₂ O ₃	14.51	13.21	14.83	14.86	14.17	13.48	14.01	7.10
Fe ₂ O ₃ T	8.92	11.65	11.40	11.00	11.95	12.42	11.93	14.14
MgO	8.13	6.45	4.91	5.15	6.24	7.78	9.74	21.69
CaO	9.10	9.82	11.82	11.98	11.41	10.80	9.19	6.80
Na ₂ O	3.22	2.74	2.93	3.05	2.69	2.68	2.16	0.87
K ₂ O	1.156	0.844	1.027	1.016	0.974	0.679	1.113	0.399
TiO ₂	2.933	2.554	3.148	3.214	3.086	2.491	2.988	1.531
MnO	0.162	0.148	0.152	0.127	0.166	0.175	0.167	0.171
P ₂ O ₅	0.436	0.312	0.457	0.465	0.446	0.313	0.432	0.223
LOI	2.53	0.55	1.63	1.20	1.99	1.76	2.94	5.54
Total	99.85	99.67	99.53	99.43	99.49	99.68	99.81	100.02
XRF (ppm)								
Zr	207.0	181.1	232.9	237.7	231.3	166.0	203.6	110.2
Nb	32.0	29.7	36.5	38.1	36.5	25.5	35.1	18.6
Y	27.6	24.4	29.4	30.0	29.2	27.0	26.1	13.7
Sr	459.3	397.0	578.6	591.6	515.7	406.3	416.9	243.4
Rb	11.3	15.3	17.8	15.9	17.3	9.7	14.7	7.7
Zn	107.6	96	79.7	102.8	99.4	110.6	87.2	103.6
Cu	88.8	84	67	59.9	84	82.7	81	43.9
Ni	318.9	103.5	129	98.9	81.3	168.5	141.9	888
Cr	116.0	497.6	151.9	149.1	207.0	383.9	428.2	1131.8
V	313.3	269.9	280.1	294.2	267.1	234.8	282.1	135.2
Ba	171.2	183.6	218.3	225.1	194.4	150.5	206	72.4
Sc	32.1	31.3	26.2	28.5	24.8	23.6	29.9	14.1
ICP-MS (ppm)								
Y	28.28	24.57	30.35		28.80	28.59		
Zr	219.60	188.73	249.79		233.88	177.90		
Nb	31.03	28.53	37.26		35.48	25.60		
La	24.93	20.72	28.85		26.55	19.62		
Ce	57.86	47.89	65.78		61.29	45.56		
Pr	7.41	6.06	8.40		7.79	5.87		
Nd	31.04	25.65	35.72		33.16	25.10		
Sm	7.11	5.89	8.07		7.49	6.12		
Eu	2.31	1.94	2.60		2.42	2.03		
Gd	6.96	5.91	7.69		7.16	6.34		
Tb	1.03	0.89	1.13		1.07	0.99		
Dy	5.50	4.80	5.94		5.65	5.45		
Ho	1.05	0.93	1.11		1.08	1.05		
Er	2.65	2.38	2.79		2.67	2.68		
Yb	2.03	1.86	2.07		2.01	2.06		
Lu	0.28	0.25	0.28		0.28	0.29		
Hf	5.00	4.35	5.63		5.25	4.17		
Ta	2.01	1.81	2.51		2.31	1.66		
Th	2.51	2.20	3.00		2.65	2.00		

Seamount	Burton	Burton	Hadar	Hadar	Hadar	Hadar	Hadar	Hadar
Sample #	1376-18	1376-19	1377-1	1377-2	1377-3	1377-4	1377-5	1377-6
Site, hole	U1376A	U1376A	U1377A	U1377A	U1377A	U1377A	U1377A	U1377B
Core-section	23R-4	23R-6	3R-2	4R-2	5R-1	6R-1	6R-3	2R-2
Interval (cm)	1-6	46-53	6-11	55-61	62-67	89-94	26-32	130-137
Depth (mbsf)	177.23	180.07	16.67	26.49	34.75	44.62	46.57	11.77
Rock type	Int	C in B	L	L	L	L	L	L
Phenocrysts	Aphyric	M-OI-Cp	M-OI	Aphyric	Aphyric	Aphyric	M-OI	Aphyric
XRF (wt %)								
SiO ₂	46.89	46.75	51.16	45.15	47.17	46.57	40.06	48.41
Al ₂ O ₃	14.40	14.10	17.66	15.77	15.57	13.95	11.38	16.29
Fe ₂ O ₃ T	11.65	10.28	8.17	12.98	12.44	11.08	10.99	9.83
MgO	5.54	5.50	4.09	6.14	7.27	3.46	6.59	4.65
CaO	11.63	12.80	6.76	6.32	5.25	7.66	14.76	10.29
Na ₂ O	2.84	2.50	3.51	3.64	3.22	2.53	2.17	2.84
K ₂ O	0.935	0.898	1.70	1.15	1.53	2.49	1.51	1.76
TiO ₂	2.942	2.901	3.500	3.725	3.462	3.658	2.771	3.467
MnO	0.153	0.149	0.055	0.073	0.079	0.085	0.154	0.107
P ₂ O ₅	0.401	0.411	0.524	0.535	0.549	0.578	0.560	0.551
LOI	2.67	3.12	2.73	3.97	3.41	7.46	8.91	1.38
Total	100.05	99.41	99.86	99.46	99.95	99.51	99.85	99.56
XRF (ppm)								
Zr	211.4	213.1	272.0	266.7	278.4	285.1	271.9	280.3
Nb	32.5	35.4	43.0	45.4	45.8	47.5	46.2	44.4
Y	27.9	26.8	24.0	25.2	25.9	30.5	21.4	30.9
Sr	496.1	564.6	497.0	663.3	546.7	467.2	653.2	574.9
Rb	16.3	10.8	27.8	17.5	28.8	36.6	27.3	43.8
Zn	99.2	118	232.6	149.3	208.7	141.5	276.2	129
Cu	89.8	77.5	85.5	55.4	68.6	56.7	61.1	91.1
Ni	110.4	153.2	440.7	104.3	205	60.7	367.1	69
Cr	97.8	384.7	649.7	109.1	338.5	25.1	702.6	99.5
V	255.5	293.3	301.6	349.1	292.4	332.9	189.1	286.5
Ba	187.3	197.9	239.6	256.1	243.9	299.6	271.4	257
Sc	23.8	32.3	37.4	31.9	31.9	25.1	18.8	24.8
ICP-MS (ppm)								
Y	29.24	27.86	23.00	24.87	27.71	30.96		32.23
Zr	228.10	226.90	268.21	258.66	299.88	299.30		299.90
Nb	32.79	35.26	43.06	44.74	48.14	48.63		45.21
La	25.16	26.55	29.08	29.68	33.83	34.71		34.07
Ce	58.38	60.93	65.84	69.89	75.59	78.85		78.70
Pr	7.43	7.75	7.93	8.76	9.40	9.93		9.90
Nd	31.53	32.87	32.92	37.27	38.45	41.23		41.48
Sm	7.22	7.44	7.05	8.25	8.43	9.08		9.22
Eu	2.35	2.42	2.31	2.66	2.62	2.87		2.88
Gd	7.02	7.11	6.25	7.32	7.58	8.34		8.49
Tb	1.06	1.04	0.91	1.03	1.09	1.21		1.24
Dy	5.57	5.51	4.67	5.21	5.63	6.20		6.39
Ho	1.06	1.02	0.84	0.91	1.02	1.15		1.17
Er	2.69	2.61	2.04	2.22	2.56	2.77		2.92
Yb	2.07	1.95	1.47	1.57	1.95	2.05		2.12
Lu	0.28	0.27	0.20	0.22	0.26	0.28		0.29
Hf	5.09	5.17	5.97	5.87	6.70	6.58		6.59
Ta	-	2.24	2.44	2.60	2.92	2.98		2.85
Th	2.52	2.66	2.75	3.07	3.76	3.77		3.62

Seamount	Hadar	Hadar	Hadar
Sample #	1377-7	1377-8	1377-9
Site, hole	U1377B	U1377B	U1377B
Core-section	4R-2	4R-3	5R-4
Interval (cm)	8-12	72-79	15-18
Depth (mbsf)	19.44	20.83	31.97
Rock type	Int	Int	Int
Phenocrysts	M-OI-PI	M-PI	Aphyric

XRF (wt %)

SiO ₂	49.24	49.82	45.02
Al ₂ O ₃	16.42	16.18	15.18
Fe ₂ O ₃ T	9.61	8.68	12.18
MgO	4.16	4.27	3.72
CaO	10.14	11.30	10.68
Na ₂ O	3.21	3.20	2.89
K ₂ O	1.62	1.33	2.11
TiO ₂	3.048	2.953	3.445
MnO	0.106	0.093	0.193
P ₂ O ₅	0.437	0.372	0.569
LOI	1.92	1.39	3.80
Total	99.91	99.59	99.78

XRF (ppm)

Zr	211.7	210.8	277.7
Nb	32.3	32.1	46.9
Y	28.7	28.4	29.6
Sr	449.3	448.8	628.5
Rb	28.1	28.1	93.7
Zn	120.5	119.4	143.8
Cu	85.5	85.6	69.3
Ni	104	102.8	63.8
Cr	188.1	186.2	49.4
V	276.9	277.8	295.4
Ba	203.5	199.3	285
Sc	32.5	31.9	28.7

ICP-MS (ppm)

Y	26.46	26.65
Zr	208.51	271.22
Nb	32.03	46.94
La	21.34	30.33
Ce	51.44	70.43
Pr	6.39	8.68
Nd	27.51	36.54
Sm	6.39	7.91
Eu	2.09	2.49
Gd	6.24	7.26
Tb	0.96	1.05
Dy	5.15	5.47
Ho	0.97	1.01
Er	2.50	2.52
Yb	1.88	1.87
Lu	0.27	0.26
Hf	4.81	6.02
Ta	1.87	2.67
Th	1.90	2.26

Fe₂O₃T is total Fe reported as Fe₂O₃; LOI is loss on ignition at 1100°C

Table 2. Average values obtained during this study by XRF spectrometry for international standards BCR-1, BHVO-1, BHVO-2, BIR-1 and BE-N.

	BCR-1		BHVO-1		BHVO-2		BIR-1		BE-N	
	Mean (ppm)	RSD %								
<i>n</i>					5					
Nb	13.0		19.8		19.5	0.6	0.6		120.5	
Zr	192.5		173.6		172.6	0.2	17.9		273.1	
Y	38.1		27.1		26.8	0.6	16.5		30.2	
Sr	328.4		382.7		380.8	0.2	107.1		1371.6	
Rb	47.3		9.3		9.3	2.1	0.2		47.3	
<i>n</i>	3		3		3		3		3	
Zn	117.3	0.35	111.1	0.09	101.5	0.44	65.1	0.54	122.7	0.21
Cu	19.4	1.4	140.0	0.33	122.0	0.36	123.1	0.25	73.0	1.4
Ni	12.7	3.1	127.5	0.20	120.2	0.10	153.6	0.55	272.0	0.30
Cr	14.0	5.4	311.7	0.27	304.7	0.05	381.7	0.29	383.4	0.26
V	394.7	0.20	323.9	0.64	318.3	1.1	307.2	0.33	246.8	0.47
Ba	669.7	0.55	144.0	1.6	134.7	1.3	9.7	2.1	1038.3	0.16
Sc	30.7	1.7	34.5	1.2	33.4	2.4	40.3	0.76	24.5	3.1

Table 3. Average values obtained during this study by ICP MS for international standards BR and W2.

	BR		W2	
	Mean (ppm)	RSD %	Mean (ppm)	RSD %
<i>n</i>	<i>11</i>		<i>11</i>	
Y	30.9	3.2	22.5	2.8
Zr	278.4	5.1	89.8	2.8
Nb	122.6	4.6	7.6	2.7
La	85.0	7.7	10.7	5.1
Ce	155.9	6.0	23.6	2.8
Pr	17.6	6.2	3.0	4.4
Nd	66.8	5.6	13.0	4.0
Sm	12.2	5.6	3.3	4.1
Eu	3.7	5.9	1.1	4.9
Gd	10.2	5.1	3.7	5.1
Tb	1.3	6.0	0.63	4.9
Dy	6.3	5.9	3.8	4.7
Ho	1.1	6.2	0.80	5.0
Er	2.6	5.9	2.3	4.8
Yb	1.8	6.7	2.0	5.2
Lu	0.24	6.0	0.30	4.2
Hf	5.5	6.6	2.3	4.1
Ta	5.6	7.6	0.49	3.0
Th	10.6	9.9	2.2	6.2

Table 4 Distribution coefficients (D) used in this study

	Olivine				Orthopyroxene				Clinopyroxene				Garnet				Spinel		
	Mean D	1σ	n	ref.	mean D	1σ	n	ref.	mean D	1σ	n	ref.	mean D	1σ	n	ref.	D	n	ref.
Ce	0.0003	0.0002	3	4,5,8	0.0057	0.0032	8	4,5,8	0.0741	0.0383	23	1-8	0.0205	0.0166	11	2,3,5,7,8	0.01	1	9
Sm	0.0009	0.0005	4	4,5,8	0.0246	0.0186	8	4,5,8	0.2423	0.1550	23	1-8	0.2934	0.2714	11	2,3,5,7,8	0.01	1	9
Yb	0.0194	0.0165	4	4,5,8	0.1201	0.0673	8	4,5,8	0.3685	0.1541	22	1-8	3.7042	1.4169	11	2,3,5,7,8	0.01	1	9
Nb	0.0021	0.0028	2	4,5	0.0034	0.0021	6	4,5	0.0122	0.0137	21	1-7	0.0222	0.0195	10	2,3,5,7	0.08	1	10
Zr	0.0012	0.0018	3	4,5	0.0180	0.0069	6	4,5	0.0938	0.0664	21	1-7	0.3394	0.1311	9	3,5,7	0.06	1	10
Y	0.0055	0.0063	2	4,5	0.0623	0.0181	6	4,5	0.3382	0.1654	19	1,3-7	2.0380	0.6311	9	3,5,7	0.002	1	11

N = number of individual values of D

References: 1. Hart & Dunn (1993); 2. Hauri *et al.* (1994); 3. Johnson (1998); 4. McDade *et al.* (2003); 5. Salters *et al.* (2002); 6. Skulski *et al.* (1994); 7. Tuff & Gibson (2007); 8. McKenzie & O'Nions (1991); 9. Irving (1978); 10. Horn *et al.* (1994); 11. Elkins *et al.* (2008).